

Uncertainties on α_S in global PDF analyses

A.D. MARTIN^a, W.J. STIRLING^b, R.S. THORNE^c AND G. WATT^a

^a Institute for Particle Physics Phenomenology, University of Durham, DH1 3LE, UK

^b Cavendish Laboratory, University of Cambridge, CB3 0HE, UK

^c Department of Physics and Astronomy, University College London, WC1E 6BT, UK

Abstract

We determine the uncertainty on the strong coupling α_S due to the experimental errors on the data fitted in global analysis of hard-scattering data, within the standard framework of leading-twist fixed-order collinear factorisation in the $\overline{\text{MS}}$ scheme, finding that $\alpha_S(M_Z^2) = 0.1202^{+0.0012}_{-0.0015}$ at next-to-leading order and $\alpha_S(M_Z^2) = 0.1171^{+0.0014}_{-0.0014}$ at next-to-next-to-leading order. We investigate the interplay between uncertainties on α_S and uncertainties on parton distribution functions (PDFs). We show, for the first time, how both these sources of uncertainty can be accounted for simultaneously in calculations of cross sections, and we provide eigenvector PDF sets with different fixed α_S values to allow further studies by the general user. We illustrate the application of these PDF sets by calculating cross sections for W , Z , Higgs boson and inclusive jet production at the Tevatron and LHC.

1 Introduction

There has been a steady improvement in the precision and the variety of the data for deep-inelastic and related hard-scattering processes. Global parton analyses of these data allow the partonic structure of the proton to be quantified with ever-increasing accuracy. Analyses are now possible at next-to-next-to-leading order (NNLO) in the running strong coupling $\alpha_S(Q^2)$. Indeed, the accuracy is such that the theoretical formalism needs to consider effects at the level of 1%. One area which needs careful treatment at this level of accuracy is the strong coupling

itself. This applies both to the definition of the coupling, and to the uncertainties associated with it. The definition of α_S is not unique and different definitions can give noticeable differences in the results. In the recent “MSTW 2008” global fit [1] we changed the definition of the strong coupling compared to that used in previous “MRST” analyses. We discuss the technical details of this change in detail in the Appendix. However, the main emphasis of this article is the issue of the uncertainty on parton distribution functions (PDFs) and derived quantities such as cross sections, arising from the uncertainty in the strong coupling α_S . This is a non-trivial, and often significant, source of uncertainty which is generally not considered when extracting PDFs from global fits or when calculating uncertainties on hadronic cross sections. The interplay of the PDFs, their uncertainties and α_S is both interesting in itself and important for making precise cross section predictions, and in this paper we give the first comprehensive account of this subject.

The recent MSTW analysis [1] (using an improved definition of α_S) was based on the obtained “best-fit” values of the strong coupling. In the NLO and NNLO global PDF fits, the values were found to be $\alpha_S(M_Z^2) = 0.1202$ and 0.1171 , respectively. In addition to the best-fit PDFs and corresponding best-fit α_S values, we also determined a set of eigenvector (“error”) PDF sets, designed to span the variation in the parton distributions allowed by the uncertainties on the data included in the global fit. We introduced and used a new “dynamic tolerance” method for determining 68% or 90% confidence-level (C.L.) error PDFs, which is an extension of an earlier method introduced in the CTEQ6 analysis [2, 3, 4]. Then the prediction and corresponding uncertainty for a physical quantity F that depends on the PDFs, such as a cross section at a hadron–hadron collider, is given by $F(S_0) \pm \Delta F_{\text{PDF}}$ where¹

$$\Delta F_{\text{PDF}} = \frac{1}{2} \sqrt{\sum_{k=1}^n [F(S_k^+) - F(S_k^-)]^2}. \quad (1)$$

Here, S_0 is the central PDF set, and S_k^\pm ($k = 1, \dots, n$) are the eigenvector PDF sets, with $n = 20$ in the MSTW 2008 analysis [1]. To illustrate our method and its results, we used as examples in Ref. [1] the total cross sections for W^\pm and Z production at the Tevatron and LHC, i.e. we computed the theoretical predictions for the total cross sections and their corresponding PDF uncertainties, $\sigma \pm \Delta\sigma_{\text{PDF}}$.

However, the PDF sets obtained in this previous study are only defined for the particular values of $\alpha_S(M_Z^2)$ found by the best fit. If the user has a preferred (different) value of $\alpha_S(M_Z^2)$ then PDFs determined with that particular value in the global analysis should strictly be used. Hence, in this paper we provide best-fit PDFs for a range of values of $\alpha_S(M_Z^2)$. This is a straightforward matter of repetition. However, when considering *uncertainties* on PDFs and on physical quantities the process is more involved. The *true* theoretical uncertainty on a predicted cross section should also include a contribution from the allowed variation of α_S

¹In practice, we use slightly more precise formulae, given in Eqs. (51,52) of Ref. [1], leading to asymmetric PDF uncertainties; see also Eqs. (7) and (8) below.

about its best-fit value. This is particularly important for cross sections that at leading order are proportional to a power of the coupling, for example, $\sigma_{\text{Higgs}} \propto \alpha_S^2$ for production via gluon–gluon fusion at the Tevatron and LHC. A naïve way of doing this would be to define the overall theory error as $\Delta\sigma_{\text{th}}^2 = \Delta\sigma_{\text{PDF}}^2 + \Delta\sigma_{\alpha_S}^2$, where $\Delta\sigma_{\alpha_S}$ is the cross section variation when α_S is allowed to vary within some range, determined, for example, by its world-average error, for a fixed set of PDFs. However, it is not consistent to use different values of α_S in the partonic cross section describing the hard subprocess and in the PDF evolution. Moreover, in a global PDF analysis, there are non-negligible correlations between the PDFs and the value of the strong coupling. For example, the evolution of the structure function F_2 at small x is driven by the combination $\alpha_S g$, and so a large value of the coupling will correspond, in principle, to a smaller gluon distribution at low x . This is indeed observed in practice.

This PDF– α_S correlation has been known for some time, and indeed early global analyses derived a series of best-fit PDFs for a set of discrete α_S values spanning a given range, for example, $\alpha_S(M_Z^2) = 0.105, 0.110, \dots, 0.130$ [5]. Other relevant studies have been made by the CTEQ group [6, 7]. However, given that the precision of the data used in global analyses has increased significantly in recent years, with a corresponding reduction in the error on both the PDFs and on α_S , a more sophisticated approach is now required, that is, one in which (i) the allowed variation of α_S is determined by the data, and (ii) the correlation between the variation in α_S and in the PDFs is fully taken into account. The latter would be very difficult to achieve if $\alpha_S(M_Z^2)$ and its uncertainty were taken as externally determined quantities rather than obtained directly from the fit.

In this paper we investigate the interplay between uncertainties on α_S and uncertainties on parton distributions in the framework of the recent MSTW 2008 analysis [1]. We show how both these sources of uncertainty can be properly accounted for simultaneously in calculations of cross sections. The paper is organised as follows. In Section 2 we discuss how the description of each data set included in the global fit depends on the value of α_S . In Section 3 we determine the $\pm 1\sigma$ (that is, the 68% C.L.) and 90% C.L. uncertainties on $\alpha_S(M_Z^2)$ as determined in the NLO and NNLO global analyses. Moreover, we identify which particular data sets give the strongest constraints on the value of $\alpha_S(M_Z^2)$. In Section 4 we derive eigenvector PDF sets with $\alpha_S(M_Z^2)$ fixed at the limits of the 68% (and also 90%) C.L. uncertainty region. In Section 5 we illustrate our results using predictions for the W^\pm , Z , Higgs and inclusive jet cross sections at the Tevatron and LHC, i.e. we derive uncertainties on these cross section predictions which take both the allowed variation of α_S and the PDFs fully into account. We conclude in Section 6. Finally, we devote an Appendix to a discussion of the definition of α_S used in our recent MSTW 2008 analysis [1], and to a comparison with the earlier form used in the MRST analyses. The importance of a consistent definition is especially important at NNLO, where, in the $\overline{\text{MS}}$ scheme, the coupling $\alpha_S(Q^2)$ is discontinuous, albeit by a very small amount, as the scale Q^2 increases through the heavy flavour thresholds.

2 Description of data sets as a function of α_S

We plot the profiles of the goodness-of-fit quantity, χ_n^2 , for each data set n (comprising N data points), as the difference from the value at the *global* minimum, $\chi_{n,0}^2$, when varying $\alpha_S(M_Z^2)$; see Figs. 1–4 for the NNLO χ_n^2 profiles for each of the 29 different types of data.² The points (•) are generated for fixed values of $\alpha_S(M_Z^2)$ between 0.107 and 0.127 in steps of 0.001. These points are then fitted to a quadratic function of $\alpha_S(M_Z^2)$ shown by the solid lines. The horizontal dashed lines in the plots indicate the 68% and 90% C.L. limits for each data set, determined according to a “hypothesis-testing” criterion which we will describe below in Section 3.

We see from Figs. 1–4 that for most data sets the variation of χ_n^2 with respect to $\alpha_S(M_Z^2)$ is indeed approximately quadratic, with minima in the vicinity of the value of $\alpha_S(M_Z^2)$ determined by the global fit. However, a few data sets have minima which are significantly displaced from the global best-fit $\alpha_S(M_Z^2)$ values of 0.1171 at NNLO (or 0.1202 at NLO). For example, both the BCDMS and E665 data on $F_2^{\mu\{p,d\}}$ prefer $\alpha_S(M_Z^2)$ values around 0.110 or less. By contrast, the NMC $F_2^{\mu\{p,d\}}$ data sets prefer values somewhat larger than the global average. Note also from Fig. 3 that within the full global fit the H1 and ZEUS neutral-current (NC) reduced cross section data (mostly at small x) have minima at slightly high values of $\alpha_S(M_Z^2) \approx 0.121$, implying that slightly stronger evolution than with the overall best fit is preferred. A similar relative feature is found at NLO.

The data set that exhibits particularly anomalous behaviour, where χ_n^2 is significantly reduced for larger $\alpha_S(M_Z^2)$, is the DØ Run II $W \rightarrow \mu\nu$ charge asymmetry; see Fig. 4. We have already pointed out the difficulties of fitting these data in the standard NLO and NNLO global analyses (see Section 11.1 and Fig. 44 in Ref. [1]), with both fits yielding a $\chi_{n,0}^2$ of 25 for 10 data points. We also noted that the asymmetry is sensitive to the separation into valence and sea quarks, particularly at lower lepton p_T . Indeed, this explains the behaviour of χ_n^2 with $\alpha_S(M_Z^2)$: as $\alpha_S(M_Z^2)$ increases, the valence quarks evolve more rapidly at high x than the sea quarks, and the W asymmetry is reduced. For $\alpha_S(M_Z^2) \simeq 0.126$ at NNLO (or $\simeq 0.129$ at NLO) the decrease in χ_n^2 is approximately 15, and a good fit is obtained. However, such large $\alpha_S(M_Z^2)$ values are completely inconsistent with most of the other data sets in the global analysis (and with other determinations of α_S).

The NLO χ_n^2 profiles are similar to those at NNLO for most data sets. In Fig. 5 we compare the NLO and NNLO χ_n^2 profiles for those data sets where there are notable differences between the two fits. Specifically, the χ_n^2 profiles for the H1 and ZEUS F_2^{charm} data, the NMC/BCDMS/SLAC F_L data and the E866/NuSea pp Drell–Yan cross sections are clearly more quadratic at NNLO than at NLO, with minima closer to the best-fit values. This indicates a preference for the NNLO description, which is not so apparent if only the global best-fit values $\chi_{n,0}^2$ are known. Let us give the reasons for this, taking each of these data sets in turn. The χ_n^2 minimum for the F_2^{charm} data at NNLO is consistent with the global average value of $\alpha_S(M_Z^2)$, whereas a minimum is not even visible in the NLO plot. It was shown in Ref. [8] that at

²References for each of the data sets included in the global fit can be found in Ref. [1].

MSTW 2008 NNLO (α_s) PDF fit

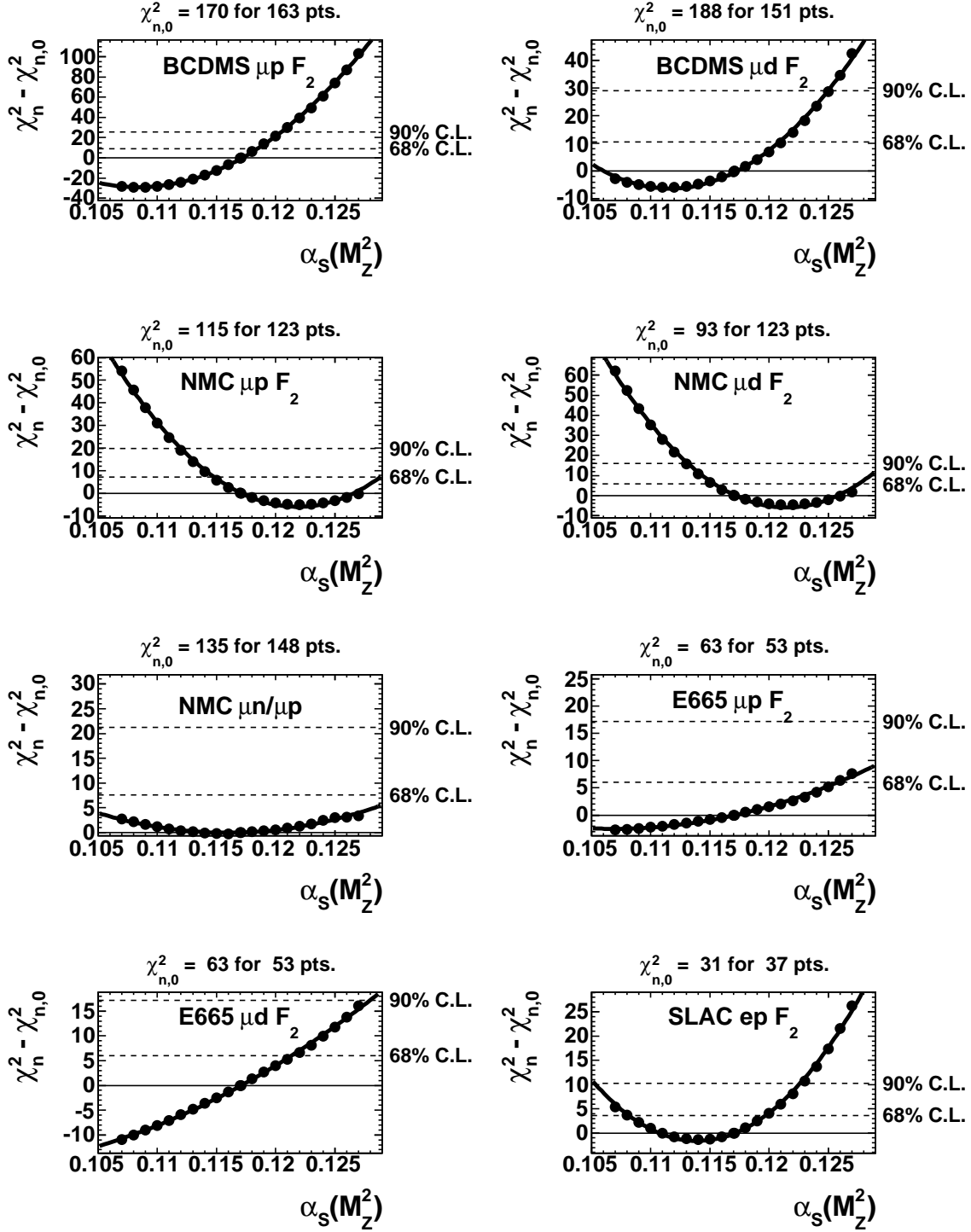


Figure 1: χ_n^2 profiles for the first subset of data sets n in the NNLO fit, when varying $\alpha_s(M_Z^2)$.

MSTW 2008 NNLO (α_s) PDF fit

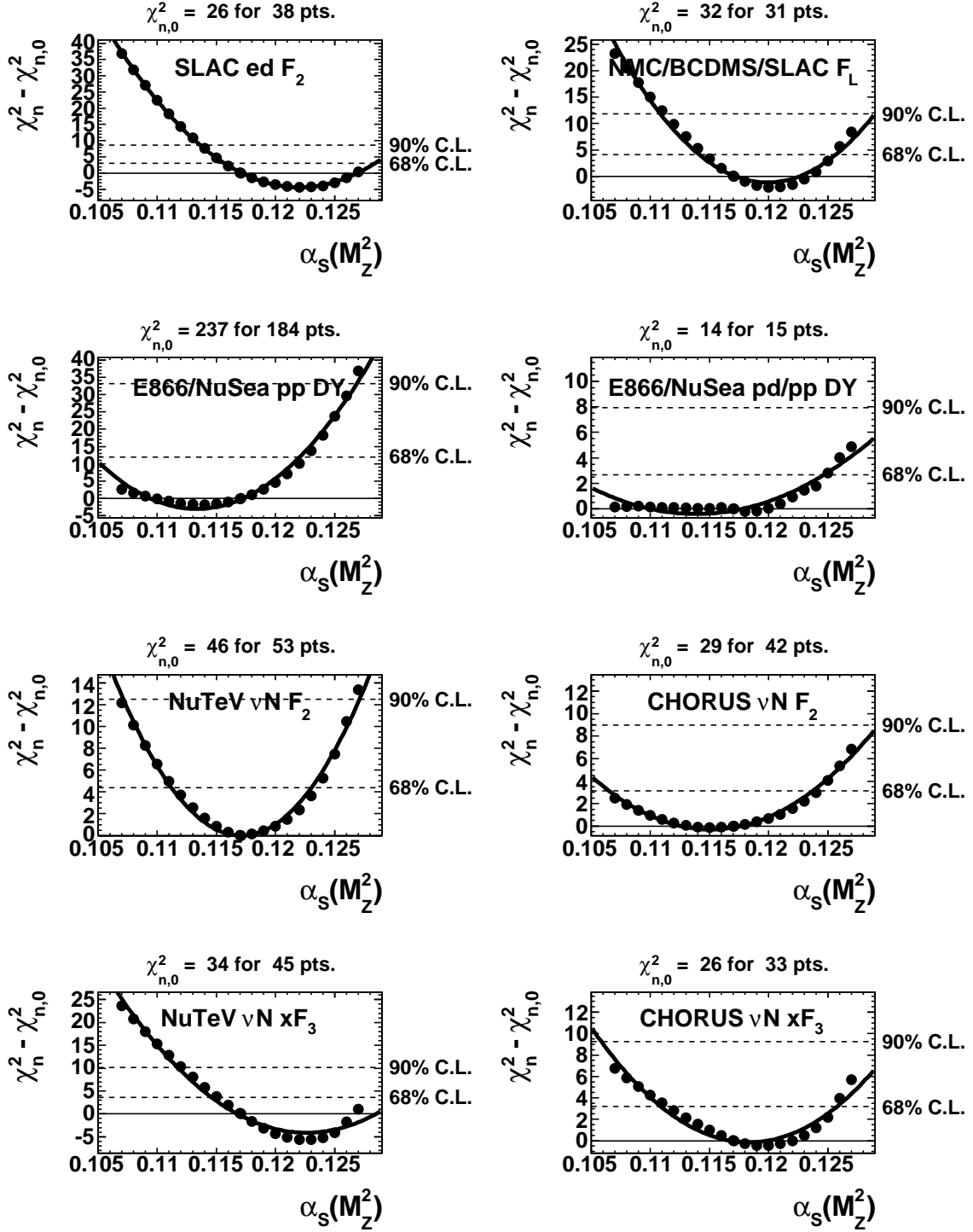


Figure 2: χ^2_n profiles for the second subset of data sets n in the NNLO fit, when varying $\alpha_s(M_Z^2)$.

MSTW 2008 NNLO (α_s) PDF fit

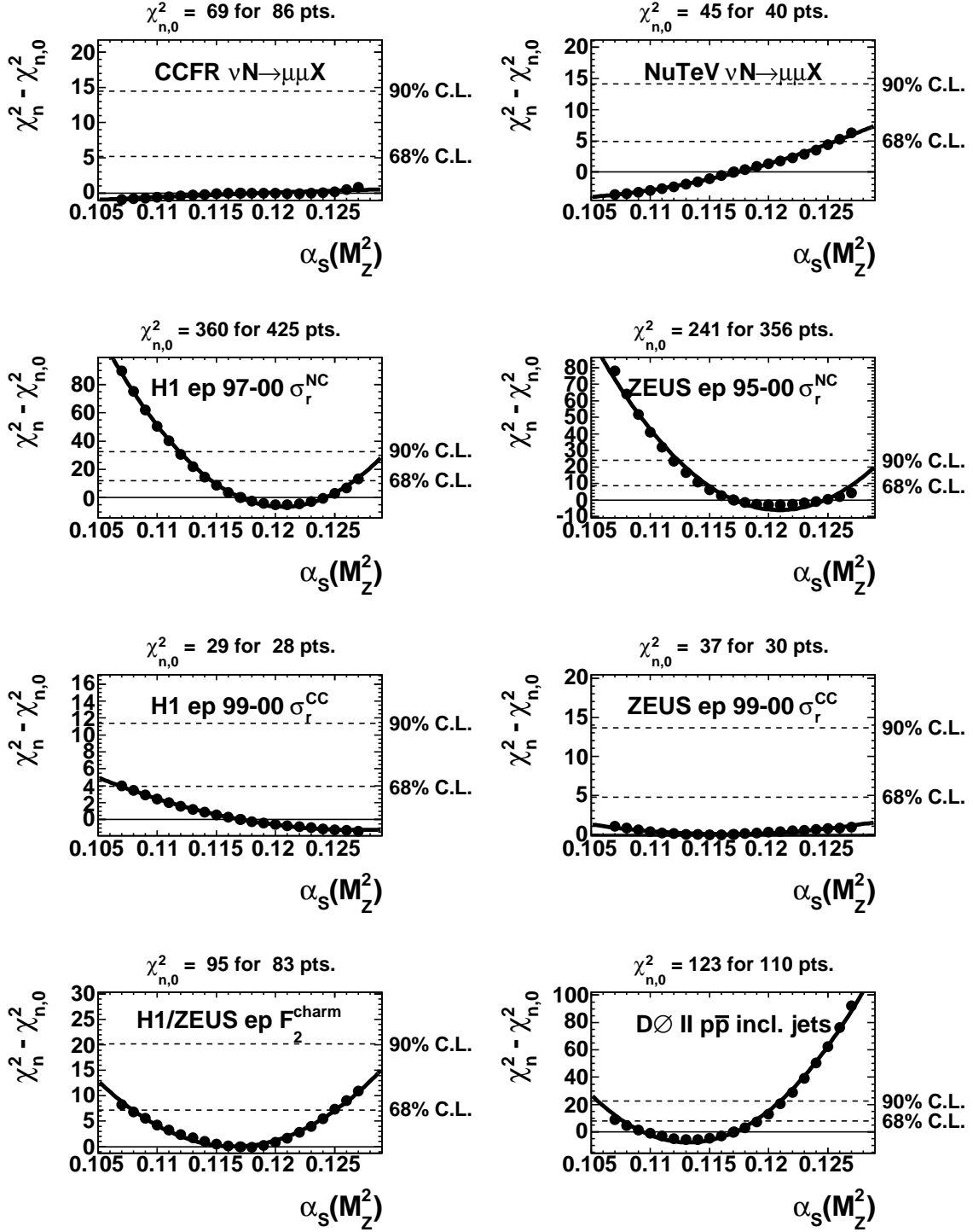


Figure 3: χ^2_n profiles for the third subset of data sets n in the NNLO fit, when varying $\alpha_s(M_Z^2)$.

MSTW 2008 NNLO (α_s) PDF fit

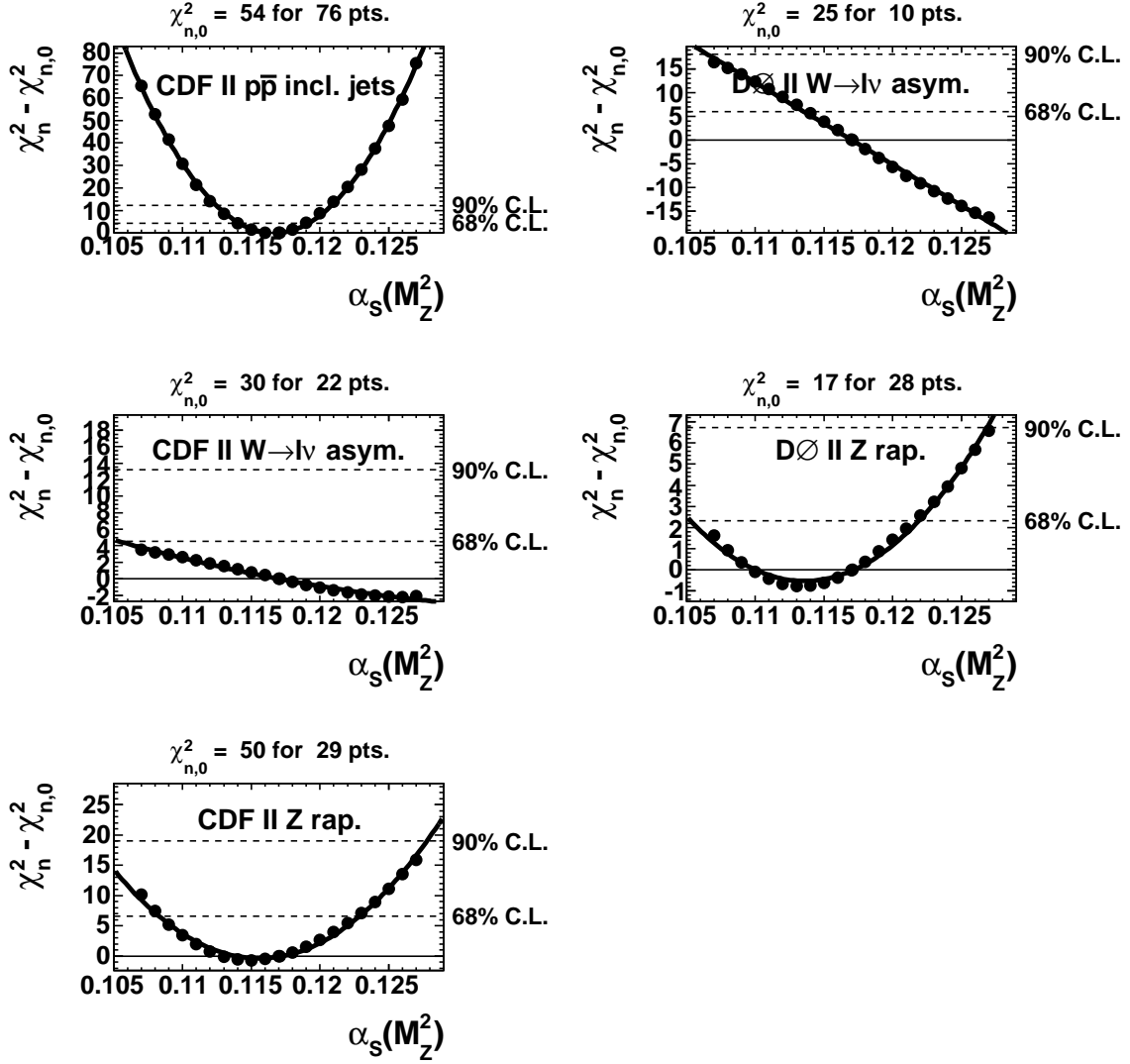


Figure 4: χ^2_n profiles for the fourth subset of data sets n in the NNLO fit, when varying $\alpha_s(M_Z^2)$.

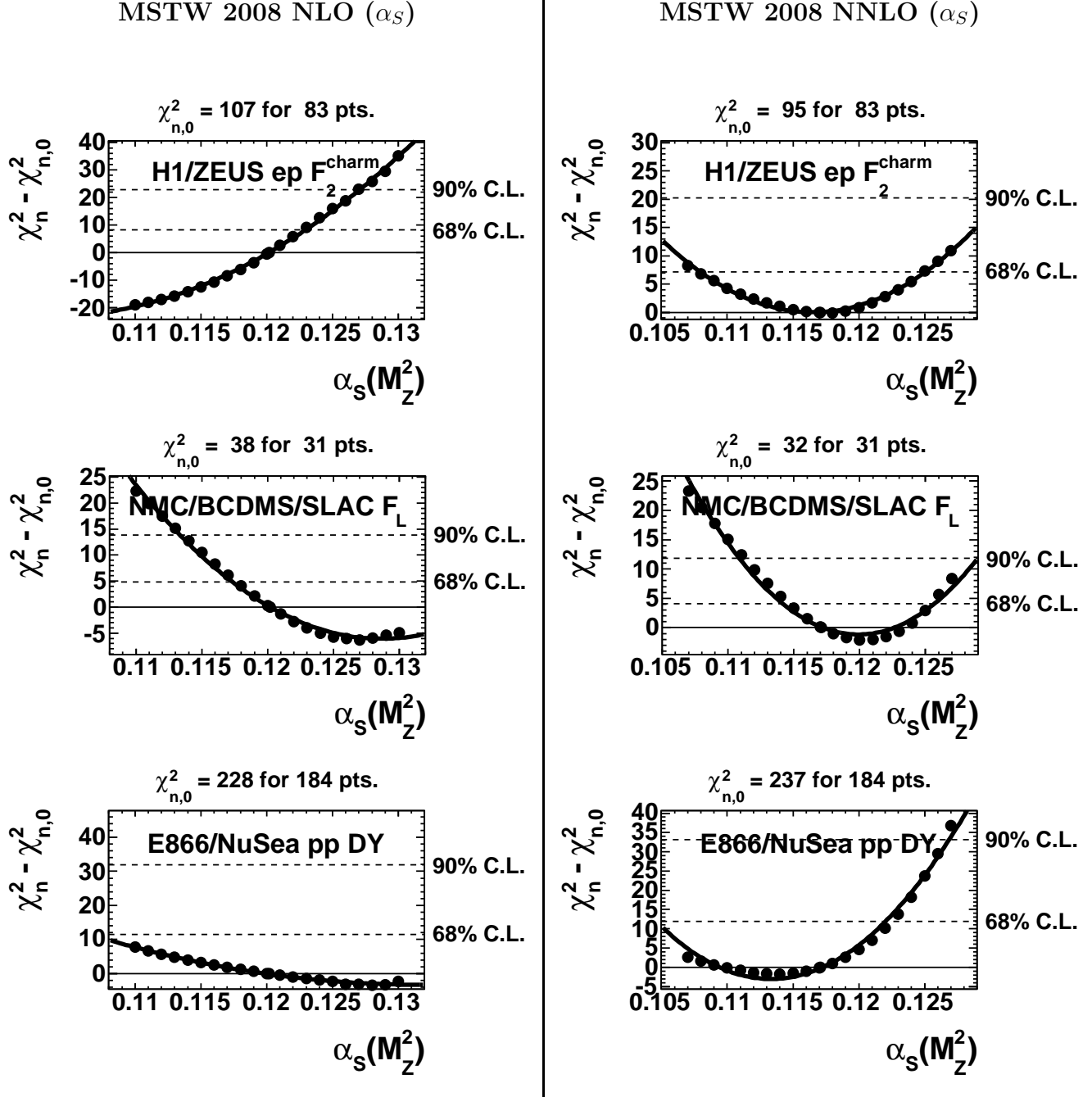


Figure 5: Comparison of selected χ_n^2 profiles in the NLO (left) and NNLO (right) fits.

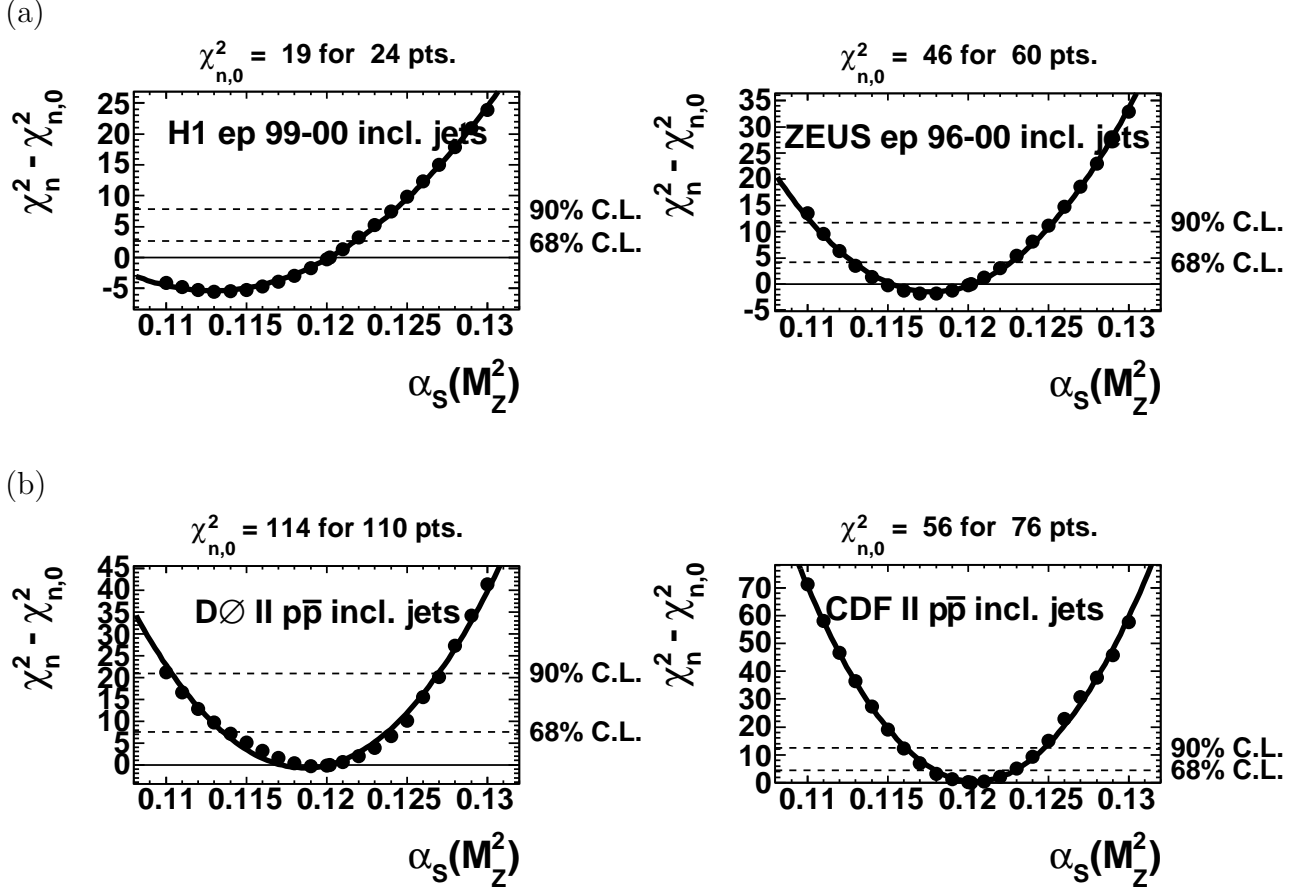


Figure 6: χ_n^2 profiles for the (a) HERA and (b) Tevatron inclusive jet production data at NLO.

NNLO the value of $\partial F_2^{\text{charm}} / \partial \ln Q^2$ is lowered compared to the NLO value. The preference of the F_2^{charm} data for this is borne out by comparing both the values of $\chi_{n,0}^2$ at each order and the shape of the profile, i.e. the NLO fit tries to flatten the slope with a lower coupling. The NNLO coefficient functions for $F_L(x, Q^2)$ [9, 10] are positive and significant, and similarly the NLO fit tries to mimic these with a higher value of $\alpha_s(M_Z^2)$. The explanation of the different profiles for the E866/NuSea pp Drell–Yan cross sections is more complicated. The positive NNLO correction [11] requires an increased data set normalisation, with a corresponding χ_n^2 penalty. However, it seems that the NNLO analysis with slightly reduced $\alpha_s(M_Z^2)$ (which marginally lowers the required normalisation penalty) gives a stable fit, whereas at NLO the increase in $\alpha_s(M_Z^2)$ makes the normalisation worse, but must improve the shape in a manner which overcompensates.

For completeness, in Fig. 6(a) we show the χ_n^2 profiles for the HERA inclusive jet production data in the NLO fit, since these H1 and ZEUS data sets are not included in the NNLO fit. Although the impact on the high- x gluon distribution is minimal, it is seen from Fig. 6 that these data sets are quite sensitive to the value of α_s , with the H1 data preferring $\alpha_s(M_Z^2) \simeq 0.113$ and the ZEUS data preferring $\alpha_s(M_Z^2) \simeq 0.118$. We also show in Fig. 6(b) the corresponding

NLO plots for the Tevatron inclusive jet production data: the preferred values of $\alpha_S(M_Z^2)$ are 0.120 for the CDF data (k_T jet algorithm) and 0.119 for the DØ data (Midpoint jet algorithm), which are very consistent with the best-fit value.

We provide public PDF grids (without uncertainties) for fits with $\alpha_S(M_Z^2)$ in the range 0.110 to 0.130 (at NLO) and 0.107 to 0.127 (at NNLO) in steps of 0.001 [12]. These grids will allow users to make α_S determinations from other data sets. Note that we have implicitly done this for each of the individual data sets in Figs. 1–6, where the values of $\alpha_S(M_Z^2)$ at the minima can be read off from the plots, together with an experimental uncertainty for an appropriate choice of $\Delta\chi_n^2 \equiv \chi_n^2 - \chi_{n,\min}^2$. (Generally, the 1- σ experimental uncertainty is taken to be the change in $\alpha_S(M_Z^2)$ which gives an increase of one unit in χ_n^2 with respect to the minimum value.) However, more detailed studies may be desirable, for example, including a theoretical uncertainty in the $\alpha_S(M_Z^2)$ determination from the observed renormalisation scale dependence. Moreover, α_S extractions from other quantities may be of interest, for example, from the ratio of three-jet to two-jet rates at the Tevatron.

Note that we do not consider LO fits in the current analysis, since the overall quality of the LO global fit of $\chi_{\text{global}}^2 = 3066$ for 2598 data points is significantly worse than those at NLO and NNLO, and therefore there is no statistically meaningful constraint on α_S at this order. As discussed in Ref. [1], the large best-fit value of $\alpha_S(M_Z^2) = 0.13939$ obtained is an attempt to mimic missing higher-order terms.

3 Experimental uncertainty on $\alpha_S(M_Z^2)$

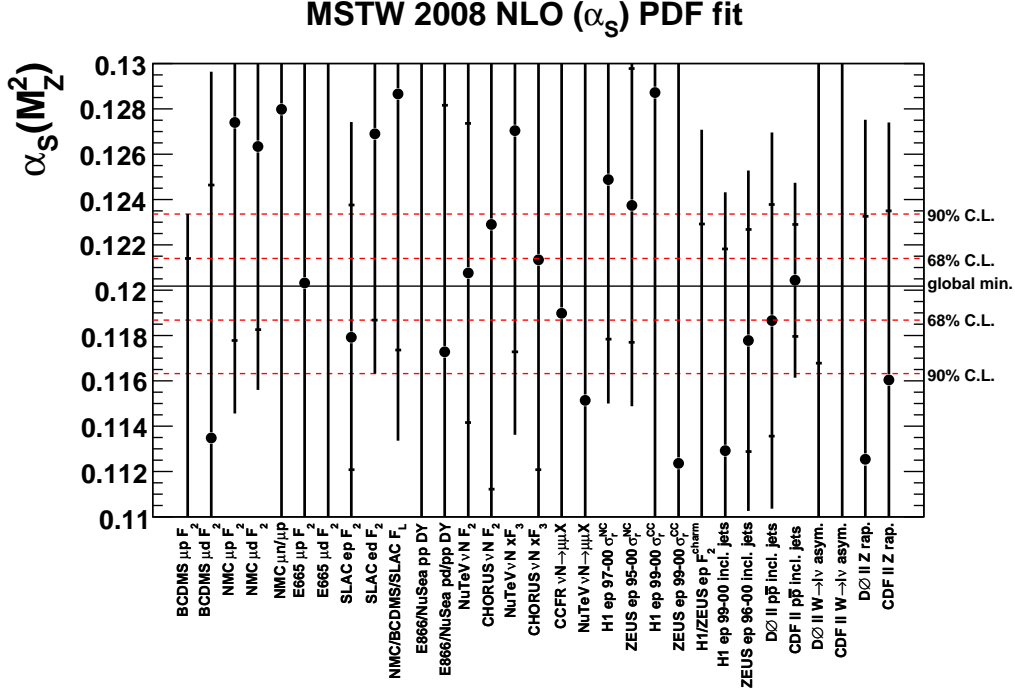
Ideally, we would expect the errors on $\alpha_S(M_Z^2)$ to be given by $\Delta\chi_{\text{global}}^2 \equiv \chi_{\text{global}}^2 - \chi_{\min}^2 = 1$ or 2.71 for a 68% or 90% C.L. limit respectively. However, in practice, there are some inconsistencies between the independent fitted data sets, so these “parameter-fitting” criteria are not appropriate for global PDF analyses. Instead, we follow the procedure of Section 6.2 of Ref. [1], where we described how to choose an appropriate value of the tolerance $T = (\Delta\chi_{\text{global}}^2)^{1/2}$ for each eigenvector of the covariance matrix according to “hypothesis-testing” criteria. Here, we will use the same method to determine the appropriate uncertainty on $\alpha_S(M_Z^2)$. To summarise, we perform the following steps.

We define the 90% C.L. region for each data set by the condition that [1]

$$\chi_n^2 < \left(\frac{\chi_{n,0}^2}{\xi_{50}} \right) \xi_{90}, \quad (2)$$

where ξ_{90} is the 90th percentile of the χ^2 -distribution with N degrees of freedom, and $\xi_{50} \simeq N$ is the most probable value. (These quantities are defined in detail in Section 6.2 of Ref. [1]; see also the example discussed around Eq. (6) below.) Similarly for the 68% C.L. region. The 90% and 68% C.L. regions determined in this way are shown as the horizontal dashed lines in Figs. 1–6. We then record the values of $\alpha_S(M_Z^2)$ for which the χ_n^2 for each data set n are

(a)



(b)

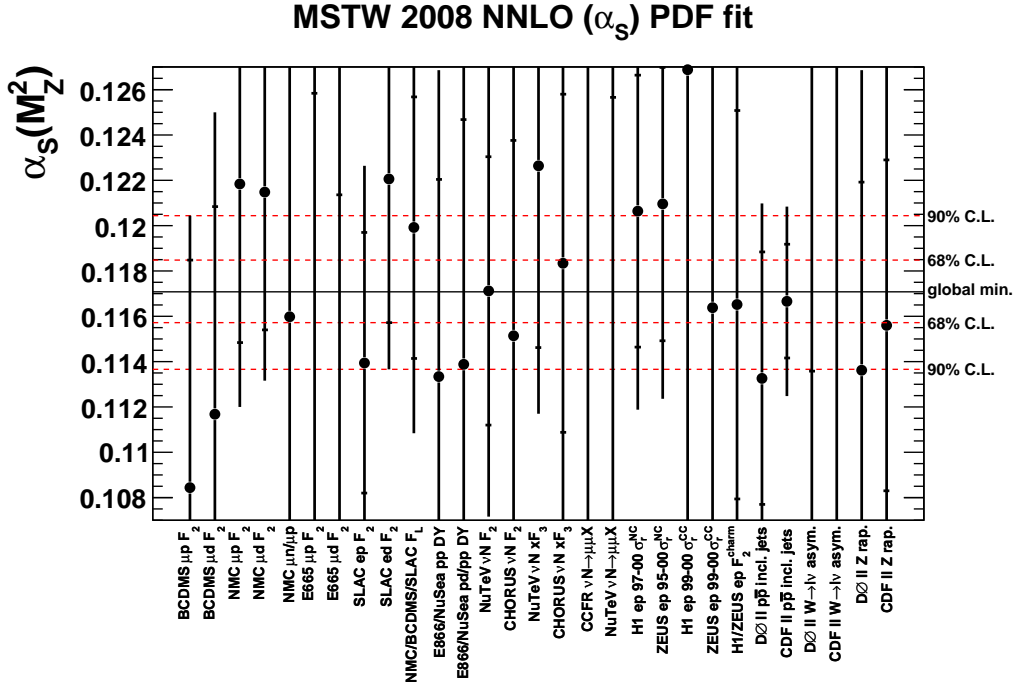


Figure 7: Ranges of $\alpha_s(M_Z^2)$ for which data sets are described within their 90% C.L. limit (outer error bars) or 68% C.L. limit (inner error bars) in the (a) NLO and (b) NNLO global fits. The points (\bullet) indicate the values of $\alpha_s(M_Z^2)$ favoured by each individual data set n , that is, the values for which χ_n^2 is minimised. The uncertainty on $\alpha_s(M_Z^2)$, indicated by the horizontal dashed lines, is chosen to ensure that all data sets are described within their 68% or 90% C.L. limits defined by Eq. (2).

minimised, together with the 90% and 68% C.L. limits defined by the intercepts of the quadratic curves with the horizontal dashed lines in Figs. 1–6.

In Fig. 7 the points (\bullet) indicate these values of $\alpha_S(M_Z^2)$ for which χ_n^2 is minimised, while the inner error bars extend across the 68% C.L. region and the outer error bars extend across the 90% C.L. region defined by Eq. (2). We choose the uncertainty on $\alpha_S(M_Z^2)$, indicated by the horizontal dashed lines in Fig. 7, so that all data sets are described within their 90% or 68% C.L. limits. It is seen from Fig. 7 that the upper limit on $\alpha_S(M_Z^2)$ is fixed by the deterioration of the quality of the fit to the BCDMS $F_2^{\mu p}$ data (within the context of the full global fit), while the lower limit is provided by the deterioration of the quality of the fit to the SLAC F_2^{ed} data. In each case a number of additional data sets are very close to providing the constraint, i.e. as with the determination of the tolerance values in Ref. [1] there is no particular reliance on any one data set in fixing the limits on $\alpha_S(M_Z^2)$. The final results are:

$$\text{NLO:} \quad \alpha_S(M_Z^2) = 0.1202 \quad {}^{+0.0012}_{-0.0015} \text{ (68\% C.L.)} \quad {}^{+0.0032}_{-0.0039} \text{ (90\% C.L.)}, \quad (3)$$

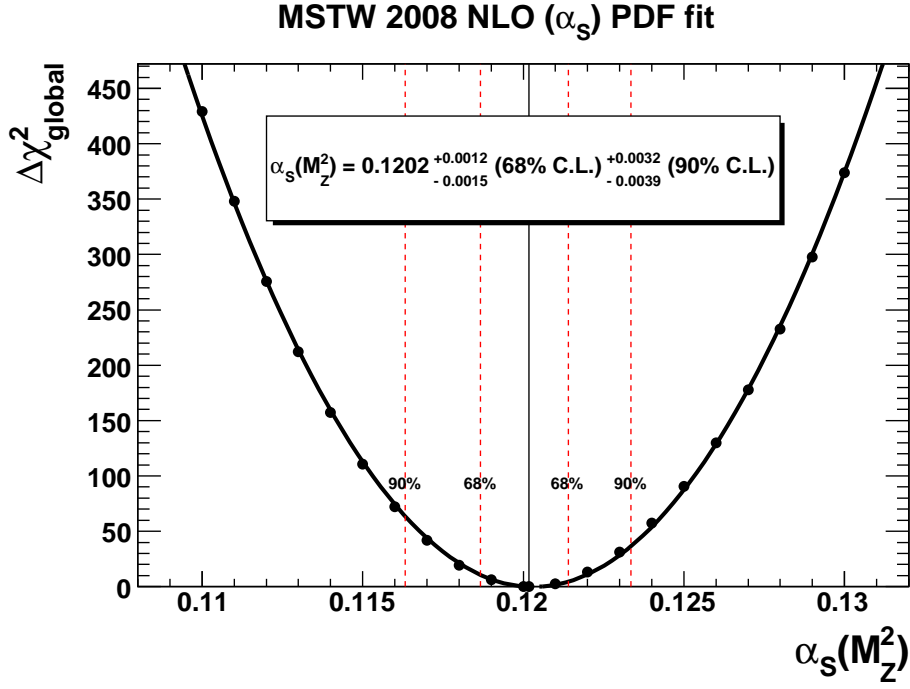
$$\text{NNLO:} \quad \alpha_S(M_Z^2) = 0.1171 \quad {}^{+0.0014}_{-0.0014} \text{ (68\% C.L.)} \quad {}^{+0.0034}_{-0.0034} \text{ (90\% C.L.)}. \quad (4)$$

In Fig. 8 we show the change in χ_{global}^2 as $\alpha_S(M_Z^2)$ is varied. The vertical lines indicate the 68% and 90% C.L. uncertainties given by Eqs. (3) and (4). The uncertainties on $\alpha_S(M_Z^2)$ at NNLO, determined using the procedure just described, amount to taking $\Delta\chi_{\text{global}}^2 = {}^{+7.6}_{-5.4}$ (68% C.L.) or ${}^{+53}_{-51}$ (90% C.L.). These are much larger values than the canonical “parameter-fitting” values of $\Delta\chi_{\text{global}}^2 = 1$ (68% C.L.) or 2.71 (90% C.L.). Conversely, if these standard “parameter-fitting” values of $\Delta\chi_{\text{global}}^2$ were taken seriously, then the uncertainties on $\alpha_S(M_Z^2)$ would be ${}^{+0.0008}_{-0.0009}$ (68% C.L.) or ${}^{+0.0010}_{-0.0011}$ (90% C.L.).

4 Eigenvector PDF sets with varying α_S

Following on from our method of determining PDF uncertainties using the Hessian method, we might consider simply letting $\alpha_S(M_Z^2)$ be another free parameter when diagonalising the covariance matrix of the fit, resulting in 42 rather than 40 eigenvector PDF sets, each with a slightly different value of α_S . We do not follow this approach for various reasons. The first of these is because the coupling does not quite sit on an equal footing with the input PDF parameters. Let us consider a superposition of different eigenvector PDF sets. The linear nature of the DGLAP evolution equations means that any linear combination of PDFs, all with a common value of $\alpha_S(M_Z^2)$, is also a well defined PDF set evolving precisely according to the DGLAP evolution equations. Consequently, the precise linear combination is the same whatever the factorisation scale at which we sample the PDFs. But if the eigenvector PDF sets in the superposition have differing $\alpha_S(M_Z^2)$, then this picture for linear combinations is not preserved. A linear combination of PDFs evolving with different $\alpha_S(M_Z^2)$ values do not evolve in precisely the same manner as one single PDF set with a fixed α_S , i.e. they do not follow precisely a real trajectory in PDF space. This is not a problem in the particular case of using

(a)



(b)

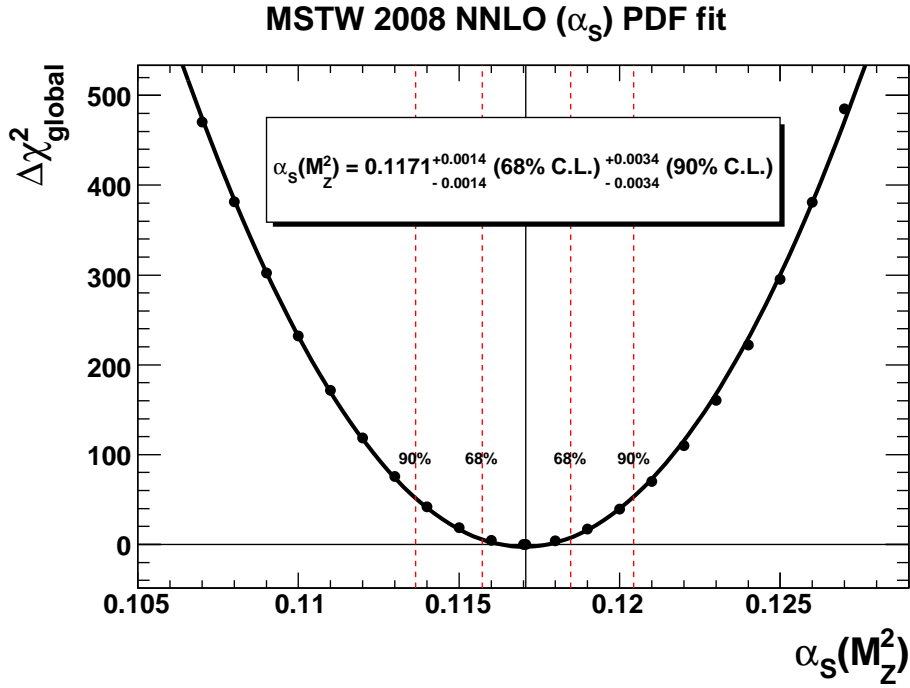


Figure 8: The points (\bullet) show $\Delta\chi_{\text{global}}^2 \equiv \chi_{\text{global}}^2 - \chi_{\text{min}}^2$ as a function of $\alpha_s(M_Z^2)$ for the (a) NLO and (b) NNLO global fits. The solid curve is a fit to a quadratic function of $\alpha_s(M_Z^2)$. The vertical dashed lines indicate the 68% and 90% C.L. uncertainties on $\alpha_s(M_Z^2)$.

the eigenvector PDF sets to map out the uncertainty band, since each is used independently. However, it is an issue when re-diagonalising the Hessian matrix, such as in Ref. [13], where, from a well-defined starting point, the new eigenvector PDF sets would not correspond to a particular PDF set which evolves in *precisely* the manner prescribed by the evolution equations. Since the whole Hessian method is based on manipulating linear combinations of perturbations in PDF parameters, which to first order in the Taylor expansion is equivalent to manipulating linear combinations of PDF sets, we find this feature troubling, even though it would certainly be a small effect in practice.

There are also more practical reasons why we reject the option of simply including α_S as an extra parameter in the Hessian matrix. We limit ourselves to 20 eigenvectors because a larger number of free input PDF parameters leads to too large correlations, and to a breakdown of the quadratic behaviour of the global χ^2 distribution in some eigenvector directions [1]. A free α_S would introduce more correlation between parameters, and reduce the stability of the eigenvectors, a feature we prefer to avoid. Finally, this approach would limit the uncertainty analysis to an expansion about the single best-fit PDF set, with a unique value of α_S . We acknowledge that the user may prefer more flexibility than this, and might wish to utilise PDF sets including uncertainties for a variety of different values of α_S . Hence, we provide eigenvector PDF sets with different, but fixed, α_S values to allow studies of this sort. In the rest of this section, we give the details of our extraction of PDFs with uncertainties at different α_S values, and examples of our recommended use of them will be given in Section 5. Here we just note that as we go away from the best-fit value of $\alpha_S(M_Z^2)$, the fit quality is automatically deteriorating, so that the PDFs cannot vary as much before the fit quality becomes unacceptable. It is an automatic result of our procedure that the PDF uncertainty shrinks as $\alpha_S(M_Z^2)$ deviates from the preferred value determined by the global fit.

We provide eigenvector PDF sets with $\alpha_S(M_Z^2)$ fixed at the limits of the 68% and 90% C.L. uncertainty regions, given by Eqs. (3) and (4). We also provide eigenvector PDF sets where $\alpha_S(M_Z^2)$ is fixed at half these limits. The eigenvector PDF sets S_k^\pm are generated, for each fixed value of α_S , from input PDF parameters [1]

$$a_i(S_k^\pm) = a_i^0 \pm t_k^\pm e_{ik}, \quad (5)$$

where a_i^0 are the best-fit input PDF parameters for that value of α_S , and the rescaled eigenvectors are $e_{ik} \equiv \sqrt{\lambda_k} v_{ik}$. The covariance (inverse Hessian) matrix has eigenvalues λ_k and orthonormal eigenvectors \mathbf{v}_k (with components v_{ik}). The distance t_k^\pm along each rescaled eigenvector direction is adjusted to give the desired tolerance $T_k^\pm = (\Delta\chi_{\text{global}}^2)^{1/2}$. In determining the tolerance for each of the eigenvector PDF sets using Eq. (2), and the corresponding equation for the 68% C.L. uncertainties, we take $\chi_{n,0}^2$ to be the values at the overall *global* minimum, that is, the values obtained using the best-fit value of $\alpha_S(M_Z^2)$.

Consider the situation when $\alpha_S(M_Z^2)$ is fixed at its *upper* 1- σ limit in the NLO fit. Recall, from Fig. 7, that this limit is fixed by the BCDMS $F_2^{\mu p}$ data set, for which $\chi_{n,0}^2 = 182.2$ for $N = 163$ degrees of freedom. In this case we have $\xi_{50} = 162.3$ and $\xi_{68} = 171.0$ (while

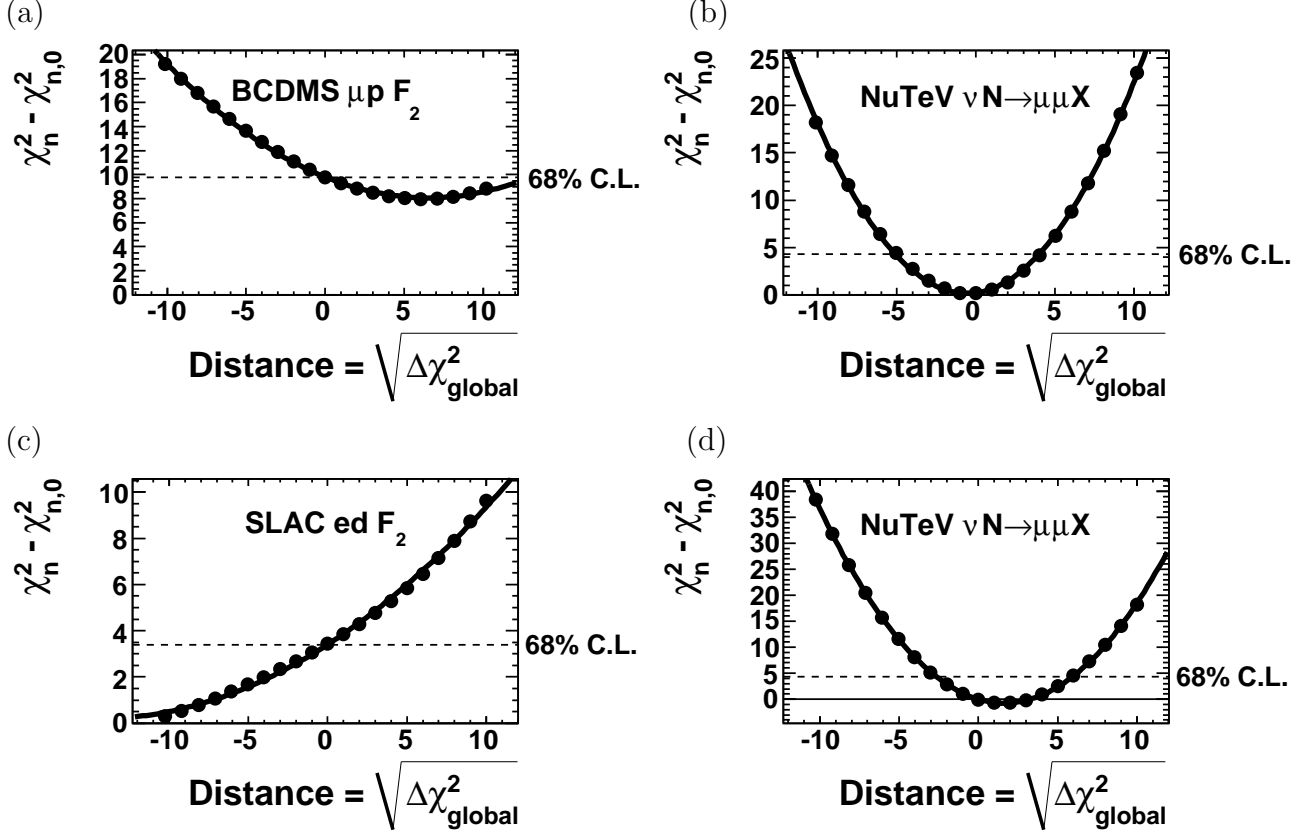


Figure 9: χ_n^2 profiles in the NLO fit when moving along eigenvector 6 for (a) the BCDMS $F_2^{\mu p}$ data when $\alpha_S(M_Z^2)$ is fixed at its *upper* 1- σ limit, (b) the NuTeV dimuon data when $\alpha_S(M_Z^2)$ is fixed at its *upper* 1- σ limit, (c) the SLAC F_2^{ed} data when $\alpha_S(M_Z^2)$ is fixed at its *lower* 1- σ limit, and (d) the NuTeV dimuon data when $\alpha_S(M_Z^2)$ is fixed at its *lower* 1- σ limit.

$\xi_{90} = 186.5$); see Fig. 7 of Ref. [1]. For this data set we define the 68% C.L. region by the condition that

$$\chi_n^2 < \left(\frac{\chi_{n,0}^2}{\xi_{50}} \right) \xi_{68}. \quad (6)$$

The rescaling factor ($\chi_{n,0}^2/\xi_{50}$) is necessary to take account of the fact that the value of $\chi_{n,0}^2$ at the global minimum is quite far from the most probable value of $\xi_{50} \simeq N$ of this data set n . Indeed, we see that in this case the best-fit value $\chi_{n,0}^2 = 182.2$ lies outside the strict 68% C.L. region $\chi_n^2 < \xi_{68} = 171.0$. After applying the rescaling factor, the 68% C.L. region is given by $\chi_n^2 - \chi_{n,0}^2 < 9.8$. That is, the central fit for the BCDMS $F_2^{\mu p}$ data, with $\alpha_S(M_Z^2)$ fixed at its upper 1- σ limit, will have χ_n^2 of 9.8 units worse than in the overall best fit. This can be clearly seen in Fig. 9(a) where we show $\chi_n^2 - \chi_{n,0}^2$ when moving along eigenvector number 6. At zero distance, $\chi_n^2 - \chi_{n,0}^2 = 9.8$, indicated by the horizontal dashed line in Fig. 9(a). Moving in the negative direction along this eigenvector, the χ_n^2 increases further, meaning that the tolerance for this eigenvector is *zero* in the negative direction. In the positive direction, the constraint which fixes the tolerance of 4.0 is provided by another data set, namely the NuTeV dimuon

data, as seen in Fig. 9(b).

In Fig. 9(c) we show the corresponding plot when $\alpha_S(M_Z^2)$ is fixed at its *lower* 1- σ limit in the NLO fit. Recall from Fig. 7 that this limit is fixed by the SLAC F_2^{ed} data, where χ_n^2 is 3.4 units worse than the best-fit value of $\chi_{n,0}^2 = 29.7$. Here, the tolerance for eigenvector number 6 is zero in the positive direction, while the constraint in the negative direction is again provided by the NuTeV dimuon data, this time giving a tolerance of 2.6, as seen in Fig. 9(d).

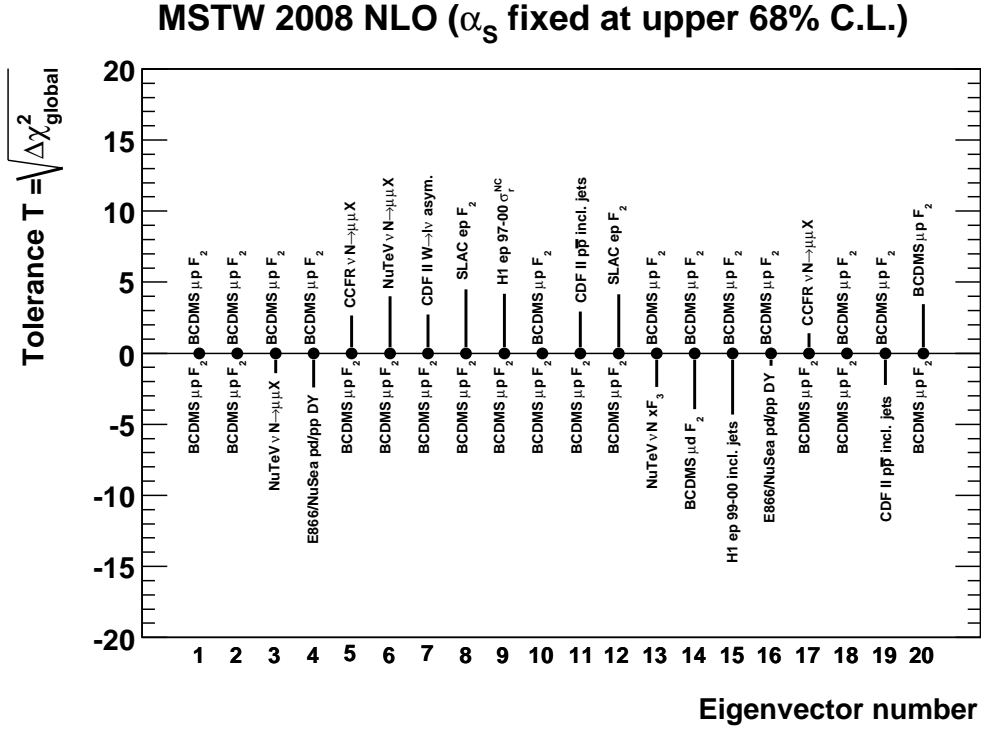
The tolerance values for each of the eigenvectors, when $\alpha_S(M_Z^2)$ is fixed at each of its 1- σ limits in the NLO fit, are shown in Fig. 10. The examples given for eigenvector number 6 were typical. However, two anomalous situations are seen to arise. Firstly, when $\alpha_S(M_Z^2)$ is fixed at its upper 1- σ limit, then the χ_n^2 for the BCDMS $F_2^{\mu p}$ data when moving along eigenvector numbers 1, 2 and 10 has a minimum (or is almost flat) at zero distance, so the tolerance is zero in both the positive and negative directions. Secondly, when $\alpha_S(M_Z^2)$ is fixed at its lower 1- σ limit, then the χ_n^2 for the SLAC F_2^{ed} data when moving along eigenvector numbers 14, 18 and 20 has a maximum at zero distance. The tolerance is then non-zero in both the positive and negative directions, since the constraint is provided by data sets other than the SLAC F_2^{ed} data. Of course, in these two anomalous situations the minima/maxima in χ_n^2 will not occur at *exactly* zero distance, and this is an artifact of working in discrete distance units of $(\Delta\chi_{\text{global}}^2)^{1/2}$, which is sufficiently accurate for our purposes.

Comparing the tolerance plots in Fig. 10 with those in Fig. 10 of Ref. [1], we see that the PDF uncertainties will be much smaller (and more asymmetric) when $\alpha_S(M_Z^2)$ is fixed at each of its 1- σ limits, compared to when it is fixed at the best-fit value. This statement is confirmed in Fig. 11 where we show the PDF uncertainties at $Q^2 = 10^4 \text{ GeV}^2$ for the cases where $\alpha_S(M_Z^2)$ is fixed at the best-fit value or shifted to each of its 1- σ limits. Note that in all cases the uncertainty bands of the PDFs when α_S is at its 1- σ limits are at most only slightly outside those for the PDFs when α_S is at its best-fit value.

There are a number of interesting features to note from Fig. 11 about the manner in which the central values of the PDFs change as a function of α_S . At high x the valence quarks (and the total up and down quark distributions) are anticorrelated with α_S . This occurs for two reasons. Firstly, the higher-order coefficient functions for structure functions in deep-inelastic scattering are positive at high x . Increasing α_S therefore means that we increase this contribution and hence require fewer quarks to fit the fixed-target structure function data at relatively low Q^2 . Secondly, the increased speed of evolution with larger α_S results in more migration from high x to lower x values. In absolute terms the effect is similar for up and down quarks, but the greater precision on up quarks means that the proportional effect is greater, and for $x \gtrsim 0.5$ the central value of the default up quark distribution is outside the error bands of the distributions generated with α_S fixed at its 1- σ limits.

Another interesting feature, seen in Fig. 11(f), is the confirmation of the anticorrelation between the small- x gluon and α_S . This is seen for x between 10^{-4} and 0.1 at $Q^2 = 10^4 \text{ GeV}^2$, and is a consequence of maintaining the fit quality to the small- x HERA data, i.e. the values of $\partial F_2 / \partial \ln Q^2 \sim \alpha_S g$. From the momentum sum rule this results in a positive correlation of

(a)



(b)

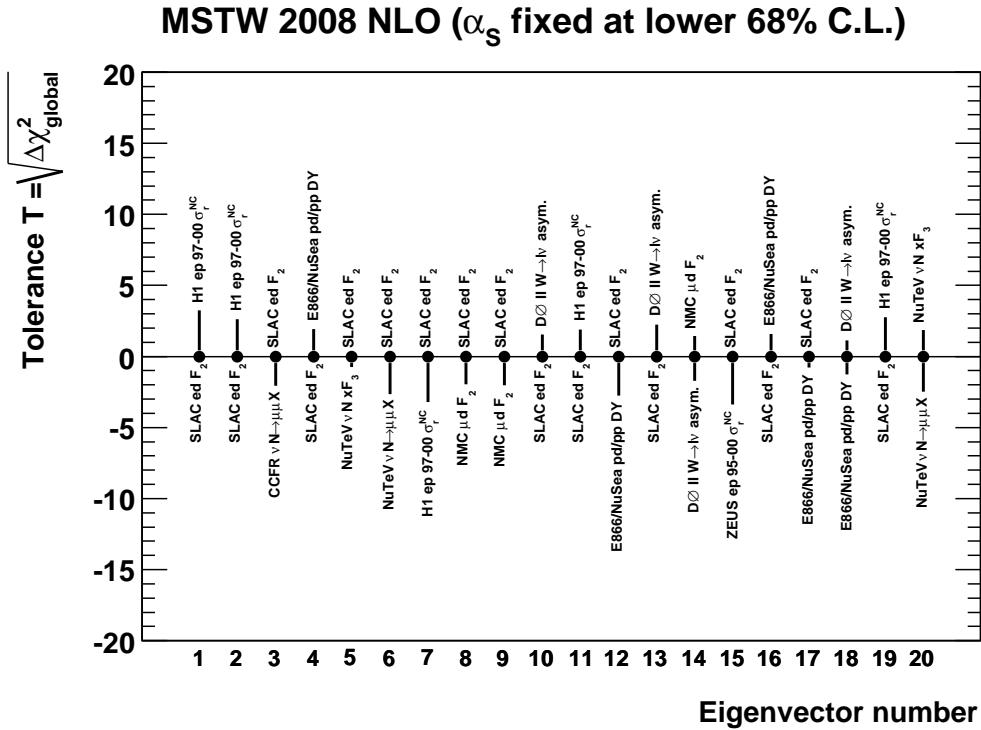


Figure 10: Tolerance values for each eigenvector when $\alpha_s(M_Z^2)$ is fixed to its (a) upper and (b) lower 1- σ limits in the NLO fit. The text labels indicate the name of the data set which sets the tolerance constraint on each eigenvector direction.

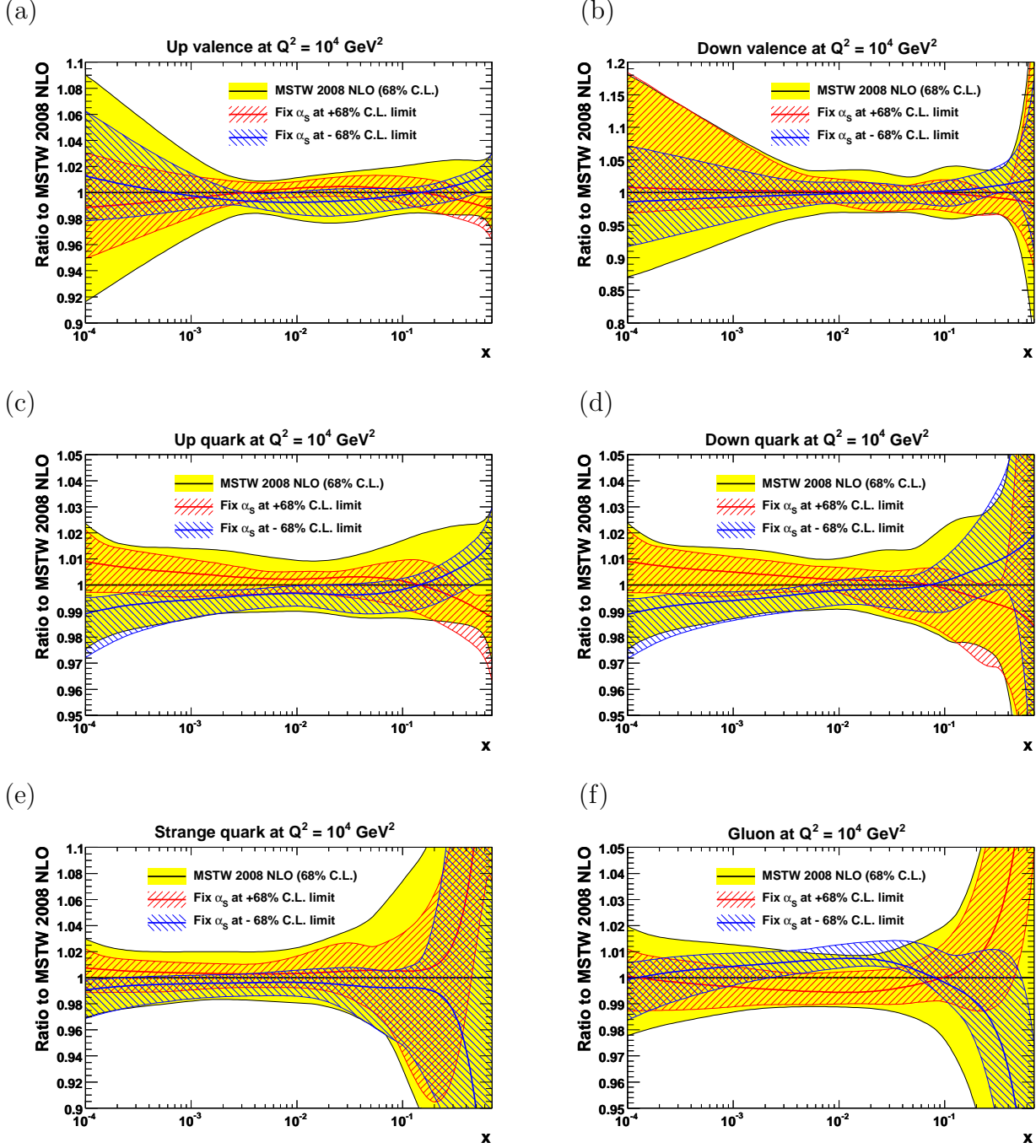


Figure 11: NLO parton distributions at $Q^2 = 10^4 \text{ GeV}^2$, including the $1\text{-}\sigma$ PDF uncertainty bands, with α_s fixed at either the best-fit value or at each of its $1\text{-}\sigma$ limits.

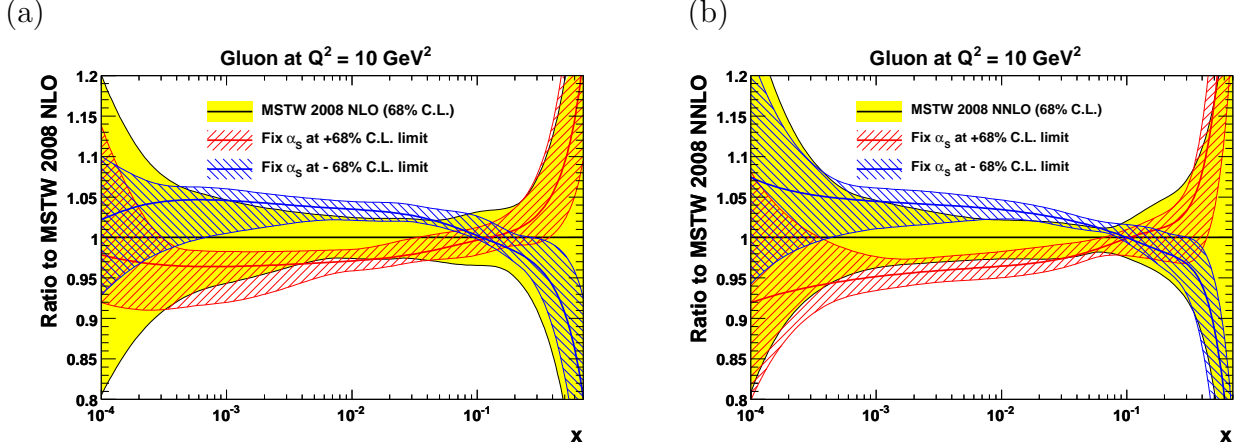


Figure 12: (a) NLO and (b) NNLO gluon distribution at $Q^2 = 10 \text{ GeV}^2$, including the $1\text{-}\sigma$ PDF uncertainty bands, with α_S fixed at either the best-fit value or at each of its $1\text{-}\sigma$ limits.

the high- x gluon and α_S . Note that there is some asymmetry in the deviation. We will return to this point in the next section. Since the quark distributions at small x are driven by the gluon, this change in the gluon affects the quarks. However, we note that there is in fact a slight *correlation* between the small- x quark distributions and α_S , showing that the increase in evolution from the increased coupling slightly outweighs the effect of the decreased small- x gluon distribution. In Fig. 12 we show similar plots for the gluon distribution at $Q^2 = 10 \text{ GeV}^2$ in both the NLO and NNLO fits. One can see that, in relative terms, the PDFs at the $1\text{-}\sigma$ limits for α_S are further from the best-fit values at $Q^2 = 10 \text{ GeV}^2$ than at $Q^2 = 10^4 \text{ GeV}^2$, although the error bands always overlap. This just illustrates that DGLAP evolution drives PDFs together at asymptotic values of Q^2 .

5 Implications for cross section calculations

To calculate uncertainties on an observable such as a hadronic cross section, the PDF uncertainty should be calculated for each of the PDF sets obtained with the five different fixed values of α_S (i.e. the best-fit α_S , α_S fixed at the two limits, and α_S at half these two limits). Then the overall “PDF+ α_S ” uncertainty on an observable can be obtained by the spread of these five individual predictions.

We now give this prescription more formally. Each fixed value of α_S is associated with a central PDF set S_0 and $2n$ eigenvector PDF sets S_k^\pm , where $k = 1, \dots, n$ and $n = 20$. An observable quantity F calculated using a particular value of α_S has a central value $F^{\alpha_S}(S_0)$ and

PDF uncertainties given by [1]

$$(\Delta F_{\text{PDF}}^{\alpha_S})_+ = \sqrt{\sum_{k=1}^n \left\{ \max \left[F^{\alpha_S}(S_k^+) - F^{\alpha_S}(S_0), F^{\alpha_S}(S_k^-) - F^{\alpha_S}(S_0), 0 \right] \right\}^2}, \quad (7)$$

$$(\Delta F_{\text{PDF}}^{\alpha_S})_- = \sqrt{\sum_{k=1}^n \left\{ \max \left[F^{\alpha_S}(S_0) - F^{\alpha_S}(S_k^+), F^{\alpha_S}(S_0) - F^{\alpha_S}(S_k^-), 0 \right] \right\}^2}, \quad (8)$$

for each of the five fixed values of α_S . Then the overall best-fit prediction is $F^{\alpha_S^0}(S_0)$, where α_S^0 is the best-fit α_S value, and the overall “PDF+ α_S ” uncertainties are given by

$$(\Delta F_{\text{PDF}+\alpha_S})_+ = \max_{\alpha_S} (\{F^{\alpha_S}(S_0) + (\Delta F_{\text{PDF}}^{\alpha_S})_+\}) - F^{\alpha_S^0}(S_0), \quad (9)$$

$$(\Delta F_{\text{PDF}+\alpha_S})_- = F^{\alpha_S^0}(S_0) - \min_{\alpha_S} (\{F^{\alpha_S}(S_0) - (\Delta F_{\text{PDF}}^{\alpha_S})_-\}). \quad (10)$$

Since this prescription might look quite complicated at first sight, we will give a few concrete examples of its application and consequences in the following subsections.³

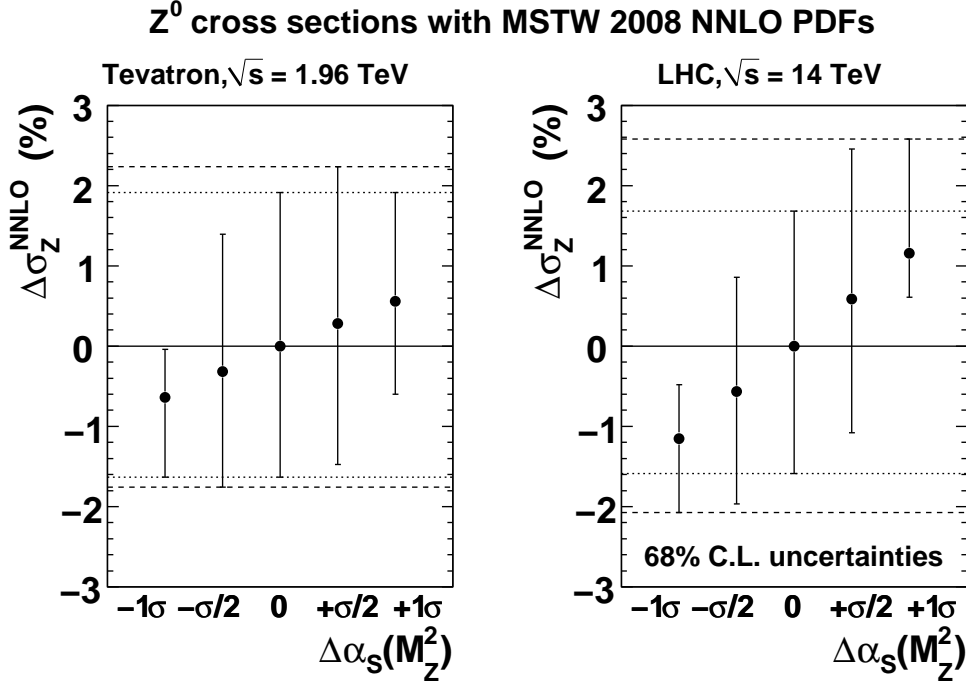
5.1 W and Z total cross sections

In Fig. 13(a) we show the PDF uncertainties on the Z total cross section at the Tevatron and LHC for each of the five sets with different fixed $\alpha_S(M_Z^2)$ values. (The situation is similar for the W^\pm cross sections.) The cross sections are calculated as described in Section 15 of Ref. [1], e.g. using the PDG 2008 [14] electroweak parameters. The increase of the Z cross section with increasing $\alpha_S(M_Z^2)$ is due to a combination of two effects. Firstly, there is the effect of the α_S dependence in the (positive) higher-order corrections to the partonic cross section. Secondly, there is the α_S dependence of the (predominantly) quark distributions. In Fig. 13(b) we show the up quark distribution at $Q^2 = M_Z^2$. The momentum fractions $x = M_Z/\sqrt{s}$ (assuming $p_T^Z = 0$, i.e. LO kinematics) probed at the Tevatron and LHC at central rapidity ($y = 0$) are indicated. As previously noted, the small- x up quark distribution is slightly correlated with the value of α_S (see also Fig. 11 for other parton flavours). However, when integrating over rapidity to obtain the total cross section, the PDFs will also be sampled at larger (and smaller) values of x . From Fig. 13(b), the up quark distribution is *anticorrelated* with α_S in the large x region, which will be sampled more at the Tevatron than at the LHC, effectively cancelling out some of the correlation with α_S arising from the sampling of smaller x values. This explains why there is less dependence on α_S at the Tevatron compared to the LHC in Fig. 13(a).

We also indicate in Fig. 13(a) how the spread of the five individual predictions can be used to give an overall uncertainty, which is larger than that obtained when $\alpha_S(M_Z^2)$ is fixed at the global best-fit value (as is usually done). Note that the extreme values for the Z cross section at the Tevatron arise when $\alpha_S(M_Z^2)$ is shifted to half its 1- σ limit. In general, there exists a

³We also provide a Fortran example program at Ref. [12].

(a)



(b)

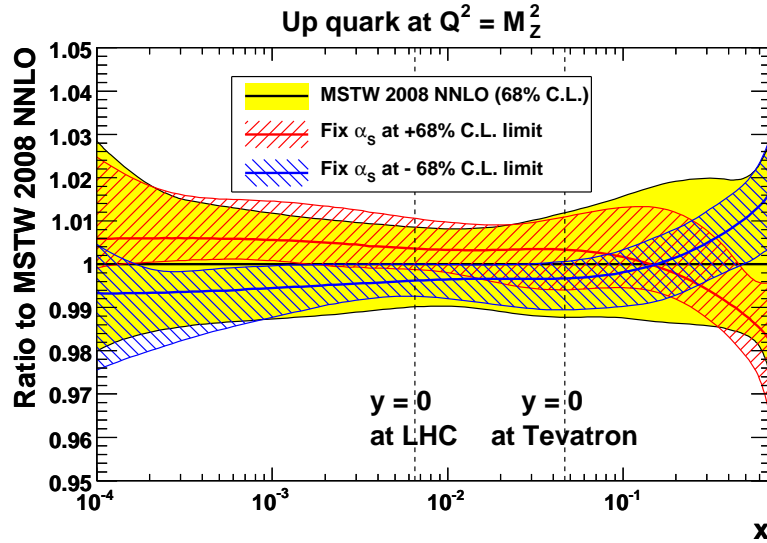


Figure 13: (a) PDF uncertainties on the Z total cross sections for each of the five PDF sets obtained from global fits performed with different fixed values of $\alpha_S(M_Z^2)$ around the best-fit value $\Delta\alpha_S(M_Z^2) = 0$. The results are shown as the percentage difference from the overall best-fit value. The horizontal dotted (dashed) lines indicate the PDF (PDF+ α_S) 68% C.L. percentage uncertainty on σ_Z . The W^\pm case is very similar. (b) NNLO up quark distribution at $Q^2 = M_Z^2$. The values of $x = M_Z/\sqrt{s}$ relevant for central production (assuming $p_T^Z = 0$) at the Tevatron and LHC are indicated.

| Tevatron, $\sqrt{s} = 1.96$ TeV | $B_{\ell\nu} \cdot \sigma_W$ (nb) | $B_{\ell^+\ell^-} \cdot \sigma_Z$ (nb) | R_{WZ} |
|---------------------------------|---|--|---|
| NNLO (PDF unc. only) | $2.747^{+0.049}_{-0.042} \left(\begin{smallmatrix} +1.8\% \\ -1.5\% \end{smallmatrix} \right)$ | $0.2507^{+0.0048}_{-0.0041} \left(\begin{smallmatrix} +1.9\% \\ -1.6\% \end{smallmatrix} \right)$ | $10.96^{+0.03}_{-0.03} \left(\begin{smallmatrix} +0.2\% \\ -0.2\% \end{smallmatrix} \right)$ |
| NNLO (PDF+ α_S unc.) | $2.747^{+0.060}_{-0.047} \left(\begin{smallmatrix} +2.2\% \\ -1.7\% \end{smallmatrix} \right)$ | $0.2507^{+0.0056}_{-0.0044} \left(\begin{smallmatrix} +2.2\% \\ -1.8\% \end{smallmatrix} \right)$ | $10.96^{+0.03}_{-0.03} \left(\begin{smallmatrix} +0.3\% \\ -0.3\% \end{smallmatrix} \right)$ |

| LHC, $\sqrt{s} = 10$ TeV | $B_{\ell\nu} \cdot \sigma_W$ (nb) | $B_{\ell^+\ell^-} \cdot \sigma_Z$ (nb) | R_{WZ} |
|-----------------------------|---|---|---|
| NNLO (PDF unc. only) | $15.35^{+0.26}_{-0.25} \left(\begin{smallmatrix} +1.7\% \\ -1.6\% \end{smallmatrix} \right)$ | $1.429^{+0.024}_{-0.022} \left(\begin{smallmatrix} +1.7\% \\ -1.6\% \end{smallmatrix} \right)$ | $10.74^{+0.02}_{-0.02} \left(\begin{smallmatrix} +0.2\% \\ -0.2\% \end{smallmatrix} \right)$ |
| NNLO (PDF+ α_S unc.) | $15.35^{+0.39}_{-0.31} \left(\begin{smallmatrix} +2.6\% \\ -2.0\% \end{smallmatrix} \right)$ | $1.429^{+0.037}_{-0.027} \left(\begin{smallmatrix} +2.6\% \\ -1.9\% \end{smallmatrix} \right)$ | $10.74^{+0.03}_{-0.03} \left(\begin{smallmatrix} +0.3\% \\ -0.3\% \end{smallmatrix} \right)$ |

| LHC, $\sqrt{s} = 14$ TeV | $B_{\ell\nu} \cdot \sigma_W$ (nb) | $B_{\ell^+\ell^-} \cdot \sigma_Z$ (nb) | R_{WZ} |
|-----------------------------|---|---|---|
| NNLO (PDF unc. only) | $21.72^{+0.36}_{-0.36} \left(\begin{smallmatrix} +1.7\% \\ -1.7\% \end{smallmatrix} \right)$ | $2.051^{+0.035}_{-0.033} \left(\begin{smallmatrix} +1.7\% \\ -1.6\% \end{smallmatrix} \right)$ | $10.59^{+0.02}_{-0.03} \left(\begin{smallmatrix} +0.2\% \\ -0.3\% \end{smallmatrix} \right)$ |
| NNLO (PDF+ α_S unc.) | $21.72^{+0.56}_{-0.48} \left(\begin{smallmatrix} +2.6\% \\ -2.2\% \end{smallmatrix} \right)$ | $2.051^{+0.053}_{-0.043} \left(\begin{smallmatrix} +2.6\% \\ -2.1\% \end{smallmatrix} \right)$ | $10.59^{+0.03}_{-0.03} \left(\begin{smallmatrix} +0.3\% \\ -0.3\% \end{smallmatrix} \right)$ |

Table 1: Predictions for $W \equiv W^+ + W^-$ and Z total cross sections at the Tevatron and LHC, and their ratio R_{WZ} , with PDF uncertainties only [1] and with the combined “PDF+ α_S ” uncertainty. The 68% C.L. uncertainties are given in all cases. We take $\mu_R = \mu_F = M_{W,Z}$.

$X \in [0, 1]$ such that the extreme value of a given observable (or a PDF itself) occurs when $\alpha_S(M_Z^2)$ is shifted by $X\text{-}\sigma$ from the best-fit value. Often, perhaps in most cases, $X = 1$, but in other cases $X < 1$, as we have here for Z production at the Tevatron. However, we see from Fig. 13(a) that the extreme values of the $\pm 1\sigma$ results are not far from the extreme values of the $\pm\sigma/2$ results, and so we do not provide PDF sets at further intermediate values of $\alpha_S(M_Z^2)$ for reasons of economy.

Note that at the LHC there is an asymmetry in the extra uncertainty generated by allowing α_S to vary, with more increase in the upwards direction than downwards. This is seen to be a consequence of a similar asymmetry in the PDF uncertainty of the up quark distribution when α_S is fixed at its upper limit, shown in Fig. 13(b), with the PDF uncertainty in the relevant x region giving more freedom for upwards movement compared to the best fit than downwards. This is due to the fact that the HERA structure function data at small x would prefer a little more evolution than in the best global fit at NNLO. The HERA data therefore allow more freedom for extra evolution when α_S increases than for reduced evolution when α_S decreases.⁴

In Tables 1 and 2 we update the NNLO predictions for W^\pm and Z production at the Tevatron and LHC that were given in Ref. [1], to allow for the enlarged uncertainty when the variation of α_S is taken into account. For the NNLO total cross sections, we see that the combined “PDF+ α_S ” uncertainty is about 2% at the Tevatron and 2.5% at the LHC. This is larger than the estimate of the theoretical uncertainty obtained from scale variation which gives below 1% [11]. However, at the LHC, the sensitivity to parton distributions at x values $\lesssim 10^{-3}$ could lead to additional uncertainties which are difficult to estimate, but variations of

⁴This effect is obscured slightly in the NLO quark distribution plots shown in Fig. 11, because the $\pm 1\sigma$ limits for $\alpha_S(M_Z^2)$ itself, mainly determined by fixed-target data, are asymmetric at NLO and larger in the downwards direction, see Eq. (3), but are practically symmetric at NNLO, see Eq. (4).

| LHC, $\sqrt{s} = 10$ TeV | $B_{\ell\nu} \cdot \sigma_{W^+}$ (nb) | $B_{\ell\nu} \cdot \sigma_{W^-}$ (nb) | R_{\pm} |
|-----------------------------|--|--|---|
| NNLO (PDF unc. only) | $8.88^{+0.15}_{-0.15} \left(\begin{smallmatrix} +1.7\% \\ -1.6\% \end{smallmatrix} \right)$ | $6.47^{+0.11}_{-0.11} \left(\begin{smallmatrix} +1.7\% \\ -1.6\% \end{smallmatrix} \right)$ | $1.373^{+0.012}_{-0.010} \left(\begin{smallmatrix} +0.8\% \\ -0.7\% \end{smallmatrix} \right)$ |
| NNLO (PDF+ α_S unc.) | $8.88^{+0.23}_{-0.19} \left(\begin{smallmatrix} +2.6\% \\ -2.1\% \end{smallmatrix} \right)$ | $6.47^{+0.16}_{-0.13} \left(\begin{smallmatrix} +2.5\% \\ -2.0\% \end{smallmatrix} \right)$ | $1.373^{+0.013}_{-0.010} \left(\begin{smallmatrix} +0.9\% \\ -0.7\% \end{smallmatrix} \right)$ |

| LHC, $\sqrt{s} = 14$ TeV | $B_{\ell\nu} \cdot \sigma_{W^+}$ (nb) | $B_{\ell\nu} \cdot \sigma_{W^-}$ (nb) | R_{\pm} |
|-----------------------------|---|--|---|
| NNLO (PDF unc. only) | $12.39^{+0.22}_{-0.21} \left(\begin{smallmatrix} +1.8\% \\ -1.7\% \end{smallmatrix} \right)$ | $9.33^{+0.16}_{-0.16} \left(\begin{smallmatrix} +1.7\% \\ -1.7\% \end{smallmatrix} \right)$ | $1.328^{+0.011}_{-0.009} \left(\begin{smallmatrix} +0.8\% \\ -0.7\% \end{smallmatrix} \right)$ |
| NNLO (PDF+ α_S unc.) | $12.39^{+0.32}_{-0.28} \left(\begin{smallmatrix} +2.6\% \\ -2.3\% \end{smallmatrix} \right)$ | $9.33^{+0.24}_{-0.20} \left(\begin{smallmatrix} +2.6\% \\ -2.1\% \end{smallmatrix} \right)$ | $1.328^{+0.011}_{-0.009} \left(\begin{smallmatrix} +0.9\% \\ -0.7\% \end{smallmatrix} \right)$ |

Table 2: Predictions for W^+ and W^- total cross sections at the LHC, and their ratio R_{\pm} , with PDF uncertainties only [1] and with the combined “PDF+ α_S ” uncertainty. The 68% C.L. uncertainties are given in all cases. We take $\mu_R = \mu_F = M_W$.

PDFs from resummed fits [15] and contributions from small- x resummation to the Drell–Yan cross section [16], suggest that a few percent is quite possible.

5.2 Higgs boson total cross sections

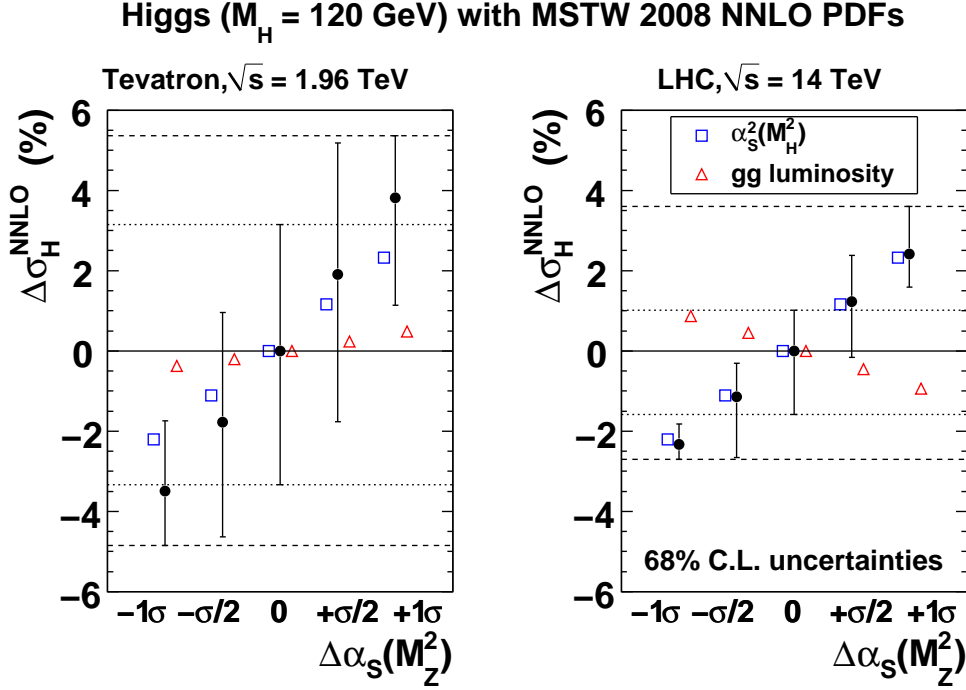
In Fig. 14(a) we show a similar plot for Higgs boson production via gluon–gluon fusion with $M_H = 120$ GeV. The Higgs cross sections are calculated using the LO subprocess $gg \rightarrow H$ via a top-quark loop (with $m_t = 175$ GeV). Higher-order corrections are included in the $m_t \rightarrow \infty$ limit up to NNLO, with only terms up to $(1-z)^1$ (where $z \equiv M_H^2/\hat{s}$) included in the expansion of the “hard” pieces of the NNLO partonic cross section around the kinematic point $z = 1$ in powers of $(1-z)$ [17] (this approximation is accurate to better than 1% [17]).

At LO, the PDF dependence of the Higgs cross section is given simply by the effective gluon–gluon luminosity, defined as

$$\frac{\partial \mathcal{L}_{gg}}{\partial M_H^2} = \frac{1}{s} \int_{\tau}^1 \frac{dx_1}{x_1} f_g(x_1, M_H^2) f_g(x_2 = \tau/x_1, M_H^2), \quad \tau = \frac{M_H^2}{s}, \quad (11)$$

while the α_S dependence of the partonic cross section is given by an overall α_S^2 factor. In Fig. 14(a) we show the percentage difference of the trivial α_S^2 factor and the gluon–gluon luminosity, with respect to the values for the best-fit α_S , for each of the five PDF sets. (The percentage PDF uncertainty on the gg luminosity for each of the five PDF sets, not shown in Fig. 14(a), is very similar to the percentage PDF uncertainty on the NNLO total cross section.) The dependence of the gg luminosity on α_S can be understood by looking at Fig. 14(b), where we show the relevant gluon distribution as a function of momentum fraction x . The momentum fractions probed at the Tevatron and LHC at central rapidity ($y = 0$), assuming LO kinematics where $p_T^H = 0$ and $x_1 = x_2 = M_H/\sqrt{s}$, are indicated. At the Tevatron, $y = 0$ corresponds almost exactly to the crossing point of the three gluon distributions shown in Fig. 14(b). However, integrating over x_1 (or equivalently, rapidity y) in Eq. (11) leads to some contribution from larger x values, leading to a slight overall correlation between the gg luminosity and α_S at

(a)



(b)

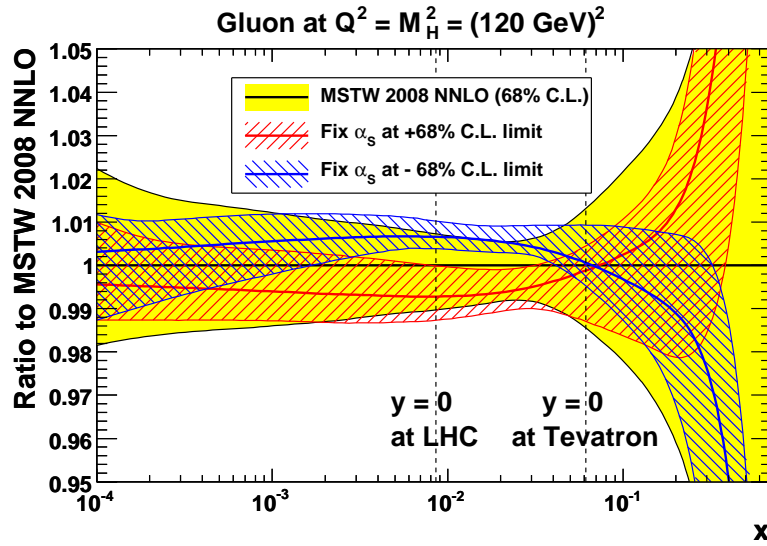


Figure 14: (a) PDF uncertainties on the Higgs total cross sections ($M_H = 120$ GeV) for each of the five PDF sets with different fixed values of $\alpha_S(M_Z^2)$. The results are shown as the percentage difference from the overall best-fit value. We also indicate the α_S dependence of the trivial α_S^2 factor and the gg luminosity (by open squares and triangles respectively, slightly offset for clarity), again shown as the percentage difference from the best-fit value. (b) NNLO gluon distribution at $Q^2 = M_H^2 = (120 \text{ GeV})^2$. The values of $x = M_H/\sqrt{s}$ relevant for central production (assuming $p_T^H = 0$) at the Tevatron and LHC are indicated.

the Tevatron. At the LHC, we see from Fig. 14(b) that $y = 0$ corresponds to the point of almost maximal anticorrelation between the gluon distribution and α_S . Again, there will be contributions from both larger and smaller x values in the integral over x_1 in Eq. (11), but there is still a substantial anticorrelation between the gg luminosity and α_S shown in Fig. 14(a). At LO, for each fixed α_S value, the percentage difference of the Higgs total cross section, with respect to the value obtained with the best-fit α_S , would be approximately given by simply adding the percentage differences of the α_S^2 factor and the gg luminosity. However, higher-order corrections will significantly increase the α_S dependence of the partonic cross section beyond the LO α_S^2 factor. We see from Fig. 14(a) that at the Tevatron both higher-order corrections and the correlation of the gg luminosity with α_S increase the α_S dependence of the Higgs total cross section. On the other hand, at the LHC, higher-order corrections compensate almost exactly for the anticorrelation of the gg luminosity with α_S , meaning that the α_S dependence of the total Higgs cross section is surprisingly almost the same as the trivial α_S^2 factor.

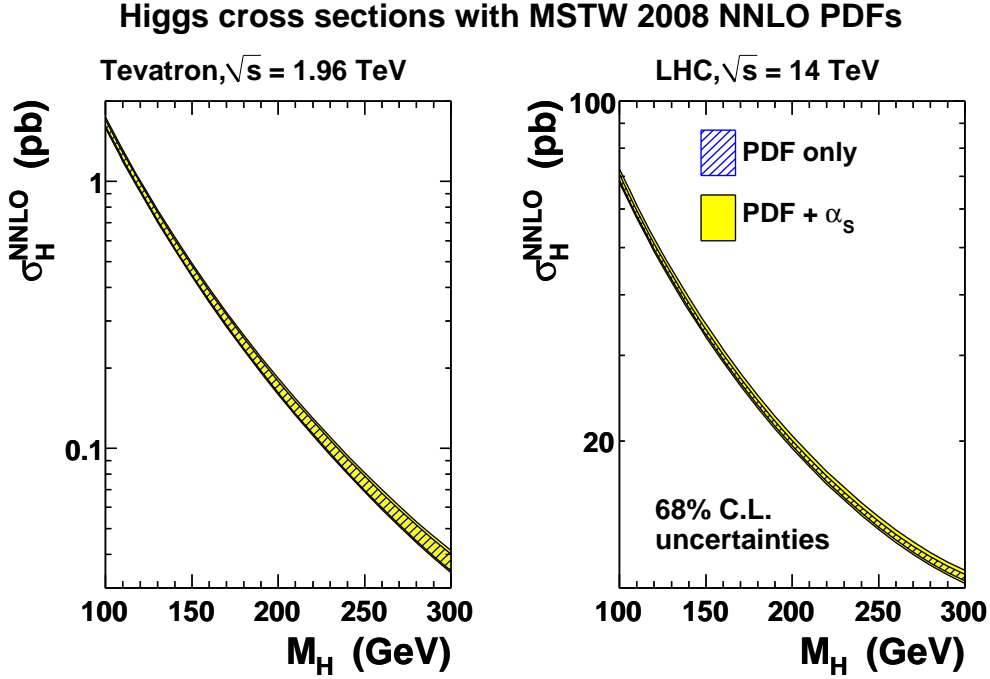
In Fig. 14(a) we also show that the “PDF+ α_S ” uncertainty, indicated by the dashed lines, is much enhanced compared to the “PDF only” uncertainty indicated by the dotted lines. Note that there is an even more marked asymmetry in the α_S dependence of the total uncertainty for Higgs production than for Z production, with much more of an increase in the upwards direction. This is due to the same source. The HERA data demand more of an increase in the gluon (with tighter bands) when α_S decreases than a decrease in the gluon when α_S increases; see Fig. 14(b). This asymmetry would be absent to first order if the default fit to the HERA structure function data was perfect.

In Fig. 15 we show, as a function of the Higgs mass, how the uncertainty increases when variation of α_S is included. Both uncertainty bands increase in size for increasing Higgs mass at the Tevatron as we become more sensitive to the less well-determined high- x gluon distribution. At the LHC, the size of the uncertainties is largely independent of the Higgs mass in the range considered here, because we are always dominated by the gluon in the region of $x \sim 10^{-2}$. The total “PDF+ α_S ” uncertainty can become comparable to the theory uncertainty estimated from scale variation (most recently updated in Refs. [18, 19]) of $\sim \pm 10\%$ for high-mass Higgs production at the Tevatron, while the uncertainty from unknown higher-order QCD corrections dominates at the LHC where the combined “PDF+ α_S ” uncertainty is still relatively small.

5.3 Inclusive jet production

In Fig. 16(a) we show the “PDF+ α_S ” uncertainty compared to the “PDF only” uncertainty as a function of p_T for inclusive jet production in a central rapidity region at the Tevatron and LHC. The inclusive jet cross sections are calculated using the FASTNLO package [21], based on NLOJET++ [22, 23], with the k_T jet algorithm. At the Tevatron we show the data-to-theory ratio for the CDF Run II data [20], where the error bars represent only the statistical uncertainties on the data, and the data points have been shifted by the correlated systematic uncertainties determined by the best-fit MSTW 2008 NLO PDFs; see Fig. 48 of [1]. Note that

(a)



(b)

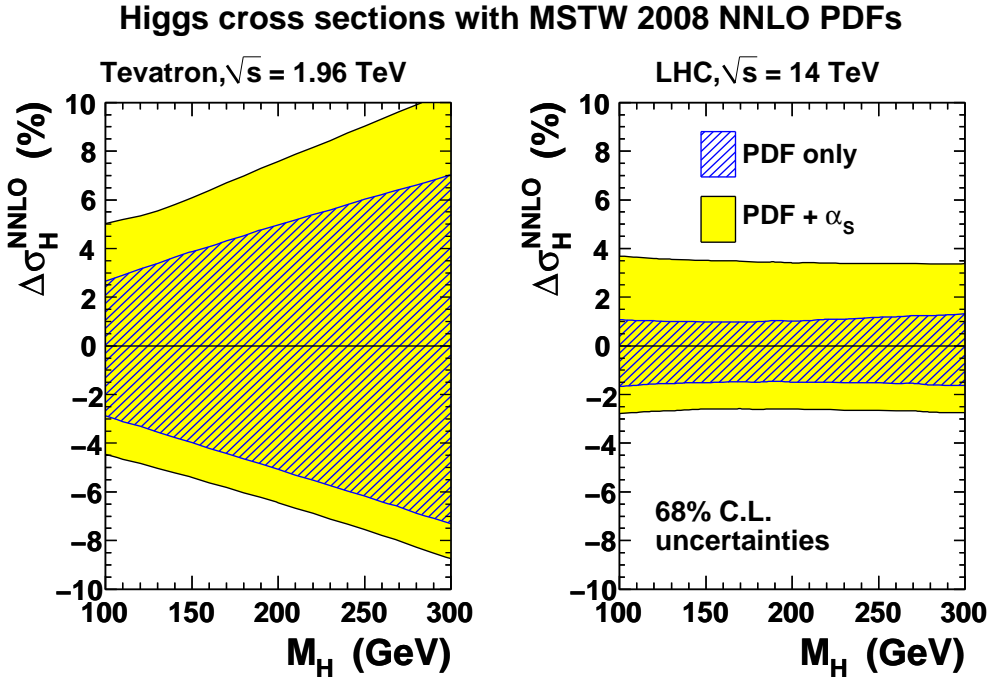
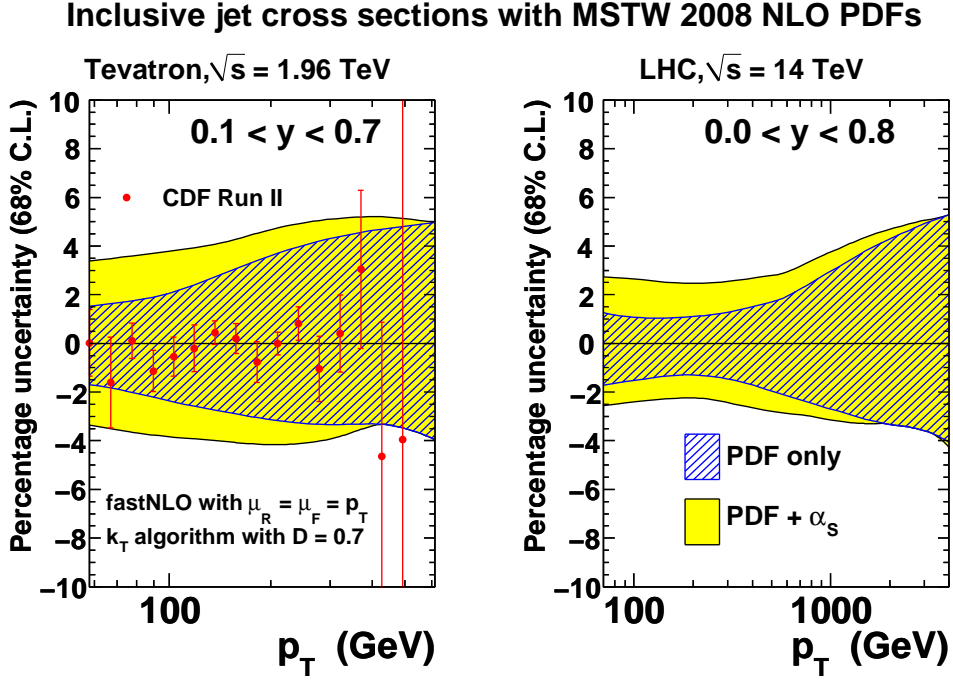


Figure 15: (a) Higgs total cross sections as a function of the Higgs mass at the Tevatron and LHC. (b) Percentage uncertainty in the Higgs total cross sections when accounting simultaneously for PDF and α_s uncertainties (outer error bands) as compared to that due to the PDF uncertainty alone (inner error bands).

(a)



(b)

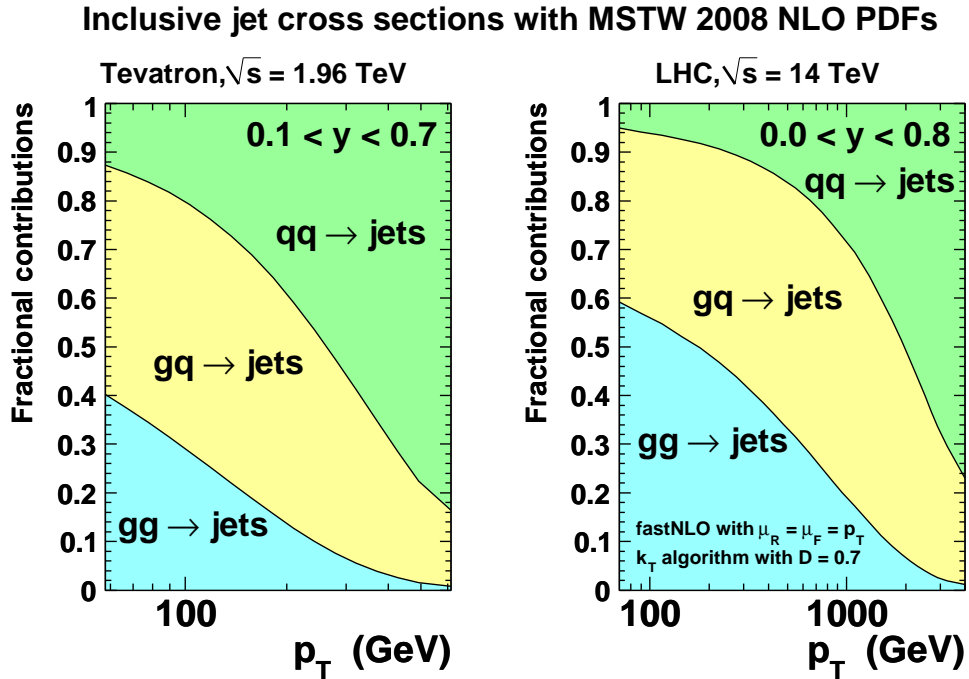


Figure 16: (a) “PDF+ α_s ” uncertainty compared to the “PDF only” uncertainty as a function of p_T for inclusive jet production in a central rapidity region at the Tevatron and LHC. At the Tevatron we also show the CDF Run II data points [20] (statistical uncertainties only). (b) Fractional contributions of the gg -, gq - and qq -initiated processes as a function of p_T .

the systematic uncertainties on the Tevatron data on inclusive jet production are generally very much larger than the statistical uncertainties. The x value probed in the PDFs is approximately $x_T = 2p_T/\sqrt{s}$, and the fractional contributions of the gg -, gq - and qq -initiated processes to the cross section are shown in Fig. 16(b). Here, gq implicitly includes qg contributions, and q stands for both quarks and antiquarks. At smaller values of p_T the additional uncertainty on α_S leads to an increase in the overall uncertainty which is due to the largely gluon-initiated cross section being correlated (or at worst uncorrelated) with α_S . At larger values of p_T , where the x probed $\gtrsim 0.3$ – 0.4 , the cross section is dominated by qq scattering. As seen in Section 4, the high- x quarks are highly anticorrelated with α_S , and hence the uncertainty on α_S does not lead to a further enhancement of the PDF uncertainty. The situation is similar in other rapidity bins. The total “PDF+ α_S ” uncertainty is smaller than the theory uncertainty at NLO estimated from scale variation, which can be $\sim \pm 10\%$. However, the PDF uncertainty tends to allow more variation in shape as a function of p_T , whereas scale variation affects mainly the normalisation (for low rapidities).

6 Conclusions

Parton distribution functions (PDFs) must be used together with the appropriate value of α_S , since both the input PDFs and $\alpha_S(M_Z^2)$ are determined simultaneously from global fits to deep-inelastic and related hard-scattering data within the framework of leading-twist fixed-order collinear factorisation (in the $\overline{\text{MS}}$ scheme). In a previous paper [1] we determined the best-fit values of $\alpha_S(M_Z^2)$ at leading-order (LO), next-to-leading order (NLO) and next-to-next-to-leading order (NNLO). In this paper we have determined the experimental uncertainties on $\alpha_S(M_Z^2)$, finding that at

$$\text{NLO:} \quad \alpha_S(M_Z^2) = 0.1202 \quad {}^{+0.0012}_{-0.0015} \text{ (68\% C.L.)} \quad {}^{+0.0032}_{-0.0039} \text{ (90\% C.L.)}, \quad (12)$$

$$\text{NNLO:} \quad \alpha_S(M_Z^2) = 0.1171 \quad {}^{+0.0014}_{-0.0014} \text{ (68\% C.L.)} \quad {}^{+0.0034}_{-0.0034} \text{ (90\% C.L.)}. \quad (13)$$

The experimental errors on α_S quoted here were obtained using an extension of the “dynamic tolerance” method [1], which gives a much refined revision on the previous estimate of ± 0.002 from the MRST 2001 analysis [24] obtained using a fixed $\Delta\chi_{\text{global}}^2 = 20$. We do not address the issue of the theory uncertainty on our α_S determination. The widely-used method of varying the renormalisation and factorisation scales up and down by a factor two is not really sufficient in a global fit, missing contributions depending on $\ln(1/x)$ and $\ln(1-x)$ at higher orders and such issues as ambiguities in heavy quark flavour scheme definitions. A simple (conservative) estimate of the theory uncertainty can be obtained by taking the difference between the NLO and NNLO determinations of $\alpha_S(M_Z^2)$. This gives a theory error of ± 0.003 , which coincides with the estimate obtained in the MRST 2001 analysis [24]. It is also of the same order as changes invoked by introducing models of higher-order corrections or changing the cuts on data at NLO [25]. It is probably an overestimate at NNLO, but more quantitative studies are needed. The values above can be compared with the world average value quoted by the

Particle Data Group (PDG) of $\alpha_S(M_Z^2) = 0.1176 \pm 0.002$ [14], where the PDG world average is dominated by NNLO results, with the NLO results included carrying little weight. We note that our $\alpha_S(M_Z^2)$ values are a little higher than those obtained in PDF determinations from mainly, or exclusively, deep-inelastic scattering data [26, 27, 28, 29].

In the process of determining the experimental uncertainty on $\alpha_S(M_Z^2)$ we performed global fits with different fixed values of $\alpha_S(M_Z^2)$ in steps of 0.001 for a range of 0.110–0.130 at NLO and 0.107–0.127 at NNLO. Public grids for these PDF sets are available from Ref. [12]. These PDF sets will be invaluable for α_S determinations by other groups.

We then considered, for the first time, the correlation between PDF uncertainties and uncertainties on $\alpha_S(M_Z^2)$. By an extension of the “dynamic tolerance” method [1] we showed how to consistently account for the effect of both these sources of uncertainty in cross section calculations. When $\alpha_S(M_Z^2)$ is fixed at either of its 1- σ limits, then the tolerance for each eigenvector PDF set will be one-sided, i.e. zero in one direction and non-zero in the other direction. Therefore, the PDF uncertainties will be much smaller (and more asymmetric) when $\alpha_S(M_Z^2)$ is fixed at either of its 1- σ limits than when $\alpha_S(M_Z^2)$ is fixed at its best-fit value. We also provide “in-between” PDF sets with $\alpha_S(M_Z^2)$ fixed at *half* the 1- σ limits, where the size of the PDF uncertainty is generally smaller than when $\alpha_S(M_Z^2)$ is at its best-fit value, but larger than when $\alpha_S(M_Z^2)$ is at its 1- σ limits. The PDF uncertainty for physical observables, such as cross sections, should be calculated separately for each of the five sets (each comprising the best-fit PDF set and 40 eigenvector PDF sets) with $\alpha_S(M_Z^2)$ displaced by $\{-1\sigma, -\sigma/2, 0, +\sigma/2, +1\sigma\}$ from its best-fit value. Then the combined “PDF+ α_S ” uncertainty is given by the envelope of these five predictions. We also provide similar 90% confidence-level (C.L.) PDF sets, where $\alpha_S(M_Z^2)$ is displaced to each of its 90% C.L. limits, and to half these limits. Public grids for all these PDF sets, for use either with the standalone MSTW interpolation code or via the LHAPDF interface [30] (from version 5.7.0), are available from Ref. [12].

As examples, we calculated the total cross sections for production of W , Z and Higgs bosons at the Tevatron and LHC. For W and Z production, where the LO subprocess is $\mathcal{O}(\alpha_S^0)$ and is quark-initiated, there is not a significant enhancement due to the combined “PDF+ α_S ” uncertainty as compared to the PDF-only uncertainty with a fixed α_S . However, the additional uncertainty due to α_S is more important for Higgs boson production via gluon–gluon fusion, where the LO subprocess is $\mathcal{O}(\alpha_S^2)$. This is particularly the case at the LHC, where the PDF uncertainty (for fixed α_S) is very small. Finally, we considered the combined “PDF+ α_S ” uncertainty on the cross sections for inclusive jet production at the Tevatron and LHC as a function of p_T . The additional uncertainty from α_S enhances the PDF-only uncertainty at low p_T , where the largely gluon-initiated cross section is correlated with α_S , but not at high p_T , where the largely quark-initiated cross section is anticorrelated with α_S .

A Appendix: Definition of $\alpha_S(Q^2)$

There is more than one definition of the strong coupling $\alpha_S(Q^2)$ beyond LO commonly used in QCD phenomenology. The various prescriptions are all formally equivalent since they differ only at higher orders. The strong coupling $\alpha_S(Q^2)$ runs according to the renormalisation group equation (RGE):

$$\frac{d}{d \ln Q^2} \left(\frac{\alpha_S}{4\pi} \right) = -\beta_0 \left(\frac{\alpha_S}{4\pi} \right)^2 - \beta_1 \left(\frac{\alpha_S}{4\pi} \right)^3 - \beta_2 \left(\frac{\alpha_S}{4\pi} \right)^4 - \dots, \quad (\text{A.1})$$

where the β -function coefficients up to NNLO are

$$\beta_0(n_f) = 11 - \frac{2}{3}n_f, \quad \beta_1(n_f) = 102 - \frac{38}{3}n_f, \quad \beta_2^{\overline{\text{MS}}}(n_f) = \frac{2857}{2} - \frac{5033}{18}n_f + \frac{325}{54}n_f^2. \quad (\text{A.2})$$

The form of $\alpha_S(Q^2)$ used in all previous MRST fits is given by

$$\alpha_S^{-1}(Q^2) = \begin{cases} \alpha_S^{-1}(Q^2, 3) + \alpha_S^{-1}(m_c^2, 4) - \alpha_S^{-1}(m_c^2, 3) & : \quad Q^2 < m_c^2 \\ \alpha_S^{-1}(Q^2, 4) & : \quad m_c^2 \leq Q^2 \leq m_b^2, \\ \alpha_S^{-1}(Q^2, 5) + \alpha_S^{-1}(m_b^2, 4) - \alpha_S^{-1}(m_b^2, 5) & : \quad Q^2 > m_b^2 \end{cases} \quad (\text{A.3})$$

where $\alpha_S(Q^2, n_f)$ is defined as the solution of the RGE, Eq. (A.1), which can be rewritten as

$$\frac{da}{d \ln Q^2} = -a^2 - b a^3 - c a^4 - \dots, \quad (\text{A.4})$$

where $a \equiv \beta_0(n_f)\alpha_S(Q^2, n_f)/(4\pi)$, $b \equiv \beta_1(n_f)/\beta_0^2(n_f)$ and $c \equiv \beta_2(n_f)/\beta_0^3(n_f)$. The solution of this equation in terms of an input parameter Λ is [31]

$$\ln \left(\frac{Q^2}{\Lambda^2} \right) = \begin{cases} \frac{1}{a} & : \quad \text{LO} \\ \frac{1}{a} - b \ln \left(\frac{1}{a} + b \right) & : \quad \text{NLO} \\ \frac{1}{a} - \frac{b^2 - 2c}{\sqrt{4c - b^2}} \tan^{-1} \left(\frac{b + 2ac}{\sqrt{4c - b^2}} \right) - b \ln \left(\frac{\sqrt{1 + ab + a^2 c}}{a} \right) & : \quad \text{NNLO} \end{cases} \quad (\text{A.5})$$

Note that $\alpha_S(Q^2)$ defined by Eq. (A.3) is continuous across the flavour thresholds, and that the fitted parameter Λ used in solving Eq. (A.5) is independent of the number of active flavours n_f . This is different from other common prescriptions where it is necessary to choose Λ to be n_f -dependent to ensure the continuity of $\alpha_S(Q^2)$. The MRST prescription, Eq. (A.3), for $\alpha_S(Q^2)$ is numerically very similar at NLO to the other two principal definitions in use, provided that the same input value $\alpha_S(M_Z^2)$ is taken [6]. However, the value of Λ determined using one prescription for $\alpha_S(Q^2)$ should not be used in a different prescription. For example, the MRST relation between Λ and $\alpha_S(Q^2)$ differs from the PDG relation [14], which also differs from the CTEQ relation [6, 7].

By differentiating Eq. (A.3) it can be shown that $\alpha_S(Q^2)$ at LO satisfies the RGE exactly, and at NLO there is an additional higher-order term of $\mathcal{O}(\alpha_S^4)$, which is sufficiently small to

be beyond the desired accuracy. Therefore, the MRST definition Eq. (A.3) is formally valid at LO and NLO, but not at NNLO. In addition, at NNLO, the strong coupling in the $\overline{\text{MS}}$ scheme is discontinuous at the heavy flavour thresholds, $Q^2 = m_H^2$, where m_H is the pole mass of the heavy quarks, i.e.

$$\alpha_S(m_H^2, n_f + 1) = \alpha_S(m_H^2, n_f) + \frac{14}{3} \left(\frac{\alpha_S(m_H^2, n_f)}{4\pi} \right)^3. \quad (\text{A.6})$$

These discontinuities in α_S were not taken into account in any of the MRST NNLO fits, including the MRST 2006 NNLO analysis [32] where the corresponding discontinuities in the PDFs were included for the first time. (It is theoretically possible to modify Eq. (A.3) to be correct up to NNLO, but only via a much more cumbersome and unattractive relationship.) Moreover, rather than use the solution of Eq. (A.5) directly, the MRST NNLO fits used a parameterisation (called **qwikalf**) of the solution as a degree-5 polynomial in $\sqrt{\ln(Q^2/\Lambda)}$, with the coefficients fitted.

We have changed the definition of α_S in the recent MSTW analyses [1] to match the definition used in public evolution codes such as PEGASUS [33] and HOPPET [34], that is, we use the exact solution of Eq. (A.1) with flavour matching using Eq. (A.6) at NNLO. (Both the MRST and MSTW definitions differ from the truncated form used by CTEQ [6, 7] and also by the PDG [14].) This change of α_S definition allowed our evolution code to be checked against the results from these two independent public evolution codes for the first time [1]. Here, for completeness, we numerically compare the MRST definition of α_S with the MSTW definition, taking the same input values of α_S at 1 GeV, 2 GeV, 10 GeV and M_Z . The input values at these scales are taken from the best-fit MSTW 2008 analyses [1] at the respective order, and the heavy flavour thresholds are set to $m_c = 1.40$ GeV and $m_b = 4.75$ GeV, evolving α_S with a maximum of five flavours. In Fig. 17 we show the ratio $\alpha_S^{\text{MRST}}/\alpha_S^{\text{MSTW}}$ as a function of the renormalisation scale $\mu_R = Q$, using, in turn, each of the four input scales. Note that $\alpha_S^{\text{MRST}} = \alpha_S^{\text{MSTW}}$ only for four flavours if the input scale is also taken in the four-flavour region. Otherwise, there are non-negligible differences. The parameterisation **qwikalf** used in the MRST NNLO fits leads to sizable discrepancies compared to the exact result given by the solution of Eq. (A.5). We see that if the MRST and MSTW analyses are forced to have the same value of α_S in the region containing the most data ($Q^2 \sim 20 \text{ GeV}^2$) then by $Q^2 = M_Z^2$ a discrepancy of more than 0.5% can occur.

References

- [1] A. D. Martin, W. J. Stirling, R. S. Thorne and G. Watt, Eur. Phys. J. C (to be published) [arXiv:0901.0002 [hep-ph]].
- [2] D. Stump *et al.*, Phys. Rev. D **65** (2002) 014012 [arXiv:hep-ph/0101051].
- [3] J. Pumplin *et al.*, Phys. Rev. D **65** (2002) 014013 [arXiv:hep-ph/0101032].

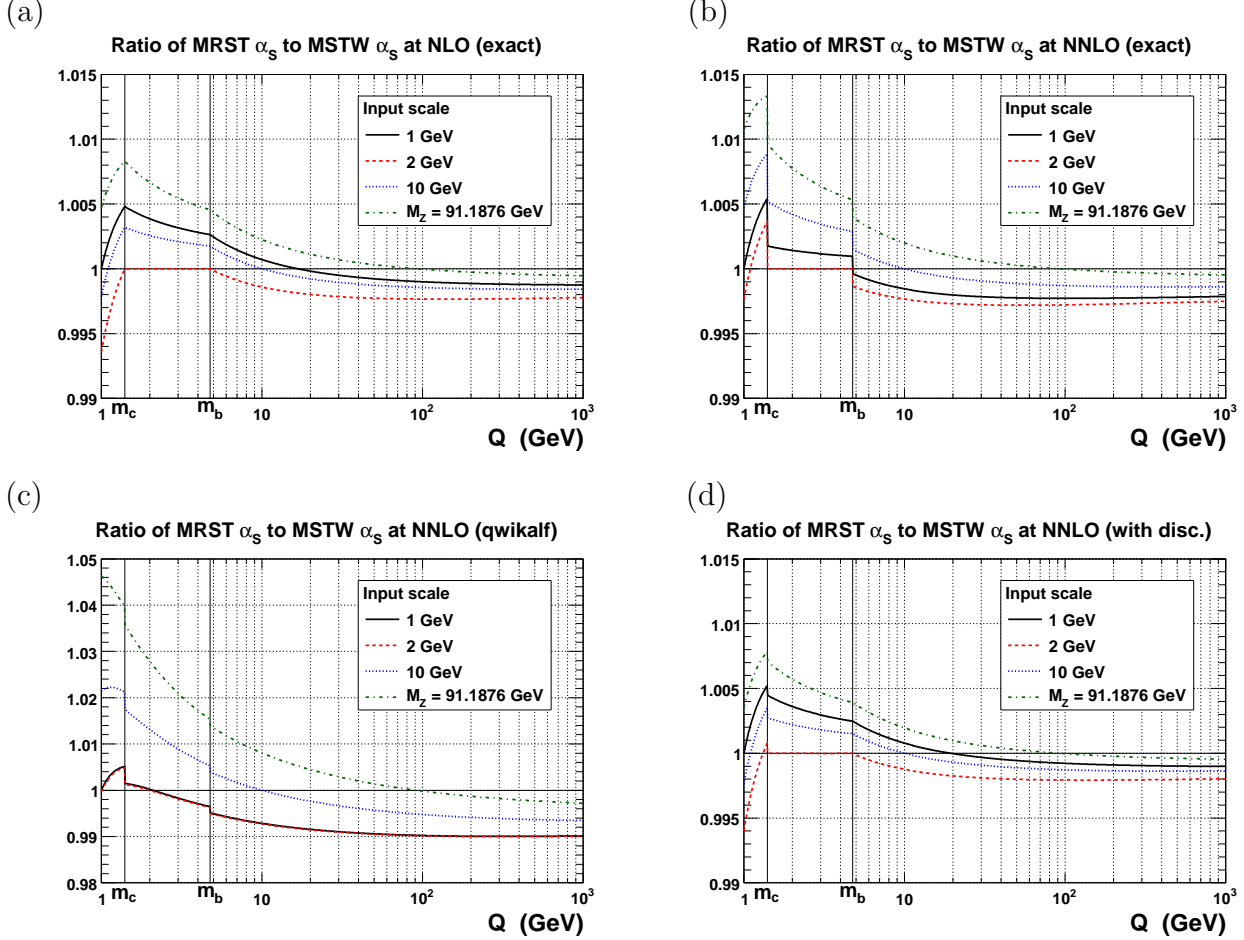


Figure 17: Ratio of the old MRST to the new MSTW α_s definitions when the common input is taken at different scales ($Q = 1$ GeV, 2 GeV, 10 GeV or M_Z), at (a) NLO and (b) NNLO. (At LO, the two definitions are identical.) The input values are taken from the MSTW 2008 best fits at the corresponding orders. The heavy flavour thresholds are at $m_c = 1.40$ GeV and $m_b = 4.75$ GeV. (c) The MRST `qwikalf` is a parameterisation of the exact result, which is clearly rather less accurate than the exact NNLO result (notice the different axis scale), but was used in all the MRST NNLO fits and is used in LHAPDF [30] with the MRST NNLO sets. (d) In principle, it is possible to add discontinuities to the MRST NNLO definition, which leads to an improvement compared to the MSTW definition.

- [4] J. Pumplin, D. R. Stump, J. Huston, H. L. Lai, P. M. Nadolsky and W. K. Tung, JHEP **0207** (2002) 012 [arXiv:hep-ph/0201195].
- [5] A. D. Martin, W. J. Stirling and R. G. Roberts, Phys. Lett. B **356** (1995) 89 [arXiv:hep-ph/9506423].
- [6] J. Huston, J. Pumplin, D. Stump and W. K. Tung, JHEP **0506** (2005) 080 [arXiv:hep-ph/0502080].
- [7] J. Pumplin, A. Belyaev, J. Huston, D. Stump and W. K. Tung, JHEP **0602** (2006) 032 [arXiv:hep-ph/0512167].
- [8] R. S. Thorne, Phys. Rev. D **73** (2006) 054019 [arXiv:hep-ph/0601245].
- [9] S. Moch, J. A. M. Vermaseren and A. Vogt, Phys. Lett. B **606** (2005) 123 [arXiv:hep-ph/0411112].
- [10] J. A. M. Vermaseren, A. Vogt and S. Moch, Nucl. Phys. B **724** (2005) 3 [arXiv:hep-ph/0504242].
- [11] C. Anastasiou, L. J. Dixon, K. Melnikov and F. Petriello, Phys. Rev. D **69** (2004) 094008 [arXiv:hep-ph/0312266].
- [12] <http://projects.hepforge.org/mstwpdf/>
- [13] J. Pumplin, arXiv:0904.2425 [hep-ph].
- [14] C. Amsler *et al.* [Particle Data Group], Phys. Lett. B **667** (2008) 1.
- [15] C. D. White and R. S. Thorne, Phys. Rev. D **75** (2007) 034005 [arXiv:hep-ph/0611204].
- [16] S. Marzani and R. D. Ball, Nucl. Phys. B **814** (2009) 246 [arXiv:0812.3602 [hep-ph]].
- [17] R. V. Harlander and W. B. Kilgore, Phys. Rev. Lett. **88** (2002) 201801 [arXiv:hep-ph/0201206].
- [18] C. Anastasiou, R. Boughezal and F. Petriello, JHEP **0904** (2009) 003 [arXiv:0811.3458 [hep-ph]].
- [19] D. de Florian and M. Grazzini, Phys. Lett. B **674** (2009) 291 [arXiv:0901.2427 [hep-ph]].
- [20] A. Abulencia *et al.* [CDF - Run II Collaboration], Phys. Rev. D **75** (2007) 092006 [Erratum-ibid. D **75** (2007) 119901] [arXiv:hep-ex/0701051].
- [21] T. Kluge, K. Rabbertz and M. Wobisch, arXiv:hep-ph/0609285;
FASTNLO code from <http://projects.hepforge.org/fastnlo/>.
- [22] Z. Nagy, Phys. Rev. Lett. **88** (2002) 122003 [arXiv:hep-ph/0110315].

- [23] Z. Nagy, Phys. Rev. D **68** (2003) 094002 [arXiv:hep-ph/0307268].
- [24] A. D. Martin, R. G. Roberts, W. J. Stirling and R. S. Thorne, Eur. Phys. J. C **23** (2002) 73 [arXiv:hep-ph/0110215].
- [25] A. D. Martin, R. G. Roberts, W. J. Stirling and R. S. Thorne, Eur. Phys. J. C **35** (2004) 325 [arXiv:hep-ph/0308087].
- [26] C. Adloff *et al.* [H1 Collaboration], Eur. Phys. J. C **30** (2003) 1 [arXiv:hep-ex/0304003].
- [27] S. Chekanov *et al.* [ZEUS Collaboration], Eur. Phys. J. C **42** (2005) 1 [arXiv:hep-ph/0503274].
- [28] J. Blumlein, H. Bottcher and A. Guffanti, Nucl. Phys. B **774** (2007) 182 [arXiv:hep-ph/0607200].
- [29] S. Alekhin, K. Melnikov and F. Petriello, Phys. Rev. D **74** (2006) 054033 [arXiv:hep-ph/0606237].
- [30] M. R. Whalley, D. Bourilkov and R. C. Group, arXiv:hep-ph/0508110;
LHAPDF code from <http://projects.hepforge.org/lhapdf/>.
- [31] R. G. Roberts, “The Structure of the Proton: Deep Inelastic Scattering”, Cambridge University Press, Cambridge, UK, 1990.
- [32] A. D. Martin, W. J. Stirling, R. S. Thorne and G. Watt, Phys. Lett. B **652** (2007) 292 [arXiv:0706.0459 [hep-ph]].
- [33] A. Vogt, Comput. Phys. Commun. **170** (2005) 65 [arXiv:hep-ph/0408244].
- [34] G. P. Salam and J. Rojo, Comput. Phys. Commun. **180** (2009) 120 [arXiv:0804.3755 [hep-ph]].